

STATE-SPACE RANGLES CELL MODEL FOR INSTRUMENT CALIBRATION

A Thesis
Submitted to the Graduate Faculty
of the
North Dakota State University
of Agriculture and Applied Science

By
Aaron James Fonseca

In Partial Fulfillment of the Requirements
for the Degree of
MASTER OF SCIENCE

Major Department:
Electrical and Computer Engineering

April 2020

Fargo, North Dakota

NORTH DAKOTA STATE UNIVERSITY

Graduate School

Title

STATE-SPACE RANGLES CELL MODEL FOR INSTRUMENT CALIBRATION

By

Aaron James Fonseca

The supervisory committee certifies that this thesis complies with North Dakota State University's regulations and meets the accepted standards for the degree of

MASTER OF SCIENCE

SUPERVISORY COMMITTEE:

Prof. Roger Green

Chair

Prof. Jacob Glower

Prof. Nikita Barabanov

Approved:

April 22, 2020

Date

Dr. Benjamin Braaten

Department Chair

ABSTRACT

It is desirable to calibrate electrochemical impedance spectroscopy (EIS) instrumentation using a Randles circuit. This presents a challenge as realistic loads, simulated by this circuit, contain theoretical components (Warburg elements) that are difficult to model. This thesis proposes a state-space solution to this problem and explores the process of realizing a digital high-accuracy approximation of a Randles circuit for the purposes of verifying and calibrating EIS instrumentation. Using Valsa, Dvořák, and Friedl's network approximation of a Warburg element, a collection of state-space relations describing the impedance of a Randles circuit are derived. From these equations the process of realizing a digital system is explored; this includes a discussion on methods of discretization, an overview of the challenges of realizing digital filters, and an analysis of the effects that finite word-length has on the accuracy of the model when using fixed-point hardware.

TABLE OF CONTENTS

ABSTRACT	iii
LIST OF TABLES	vi
LIST OF FIGURES	vii
LIST OF APPENDIX CODE-LISTINGS	ix
1. BACKGROUND	1
1.1. Electrochemical Techniques	1
1.1.1. Electrochemical Techniques in the Study of Corrosion	1
1.1.2. Tafel Extrapolation	2
1.2. The AC Impedance Method	4
1.2.1. Galvanostatic Interface	4
1.2.2. Potentiostatic Interface	5
1.2.3. Lissajous Figures	7
1.2.4. AC Bridge	7
1.2.5. Phase Sensitive Detection	8
1.3. Randles Equivalent Circuit	9
1.4. Nyquist Plots of Cell Impedance	10
1.4.1. Behavior as ω Approaches Zero	13
1.4.2. Behavior as ω Approaches Infinity	13
1.4.3. Analysis of Nyquist Plots	15
1.5. Warburg Element	15
1.6. Approximating the Warburg Element over Frequencies of Interest	18
2. MODELING A RANDES CELL IN STATE-SPACE	20
2.1. Capacitor in State-Space	21
2.2. Approximation of a Warburg Element in State-Space	21

2.3.	Randles Cell in State-Space	23
2.4.	Accuracy of the State-Space Model	25
2.4.1.	Quantifying Error	27
2.4.2.	Nyquist Plots	30
3.	METHODS OF DIGITAL IMPLEMENTATION	33
3.1.	Calculating Poles and Zeros from State-Space	33
3.2.	System Discretization	35
3.2.1.	Matched Z-Transform Method	36
3.3.	Internal Filter Structure	39
3.4.	Effects of Finite Word-Length on Accuracy	40
4.	FUTURE DIRECTION AND CONCLUSION	45
4.1.	Future Direction	45
4.1.1.	Consideration of Equipment Response	45
4.1.2.	Multi-Rate Implementation	46
4.2.	Conclusion	46
	REFERENCES	48
	APPENDIX. CODE LISTINGS	51

LIST OF TABLES

<u>Table</u>	<u>Page</u>
2.1. Test cases for different parameter values	27
3.1. Generalized input/output mapping for realization on a microprocessor with a DAC. . .	33
3.2. Test cases for different word lengths.	41

LIST OF FIGURES

Figure	Page
1.1. Tafel extrapolation of anodic and cathodic currents I_{an} and I_{ca} (Tafel lines), from experimental data I_{exp} , to determine corrosion current density at equilibrium I_{corr}	3
1.2. Basic configuration of a galvanostat. Here, current is controlled indirectly by the voltage source $u(t)$ which affects the current through the cell by means of its relationship with resistor R_i . The voltage across the cell is measured with a voltmeter and the results are logged [1, p. 38].	4
1.3. The basic configuration of a potentiostat. Here, voltage is controlled by the voltage source $u(t)$. The current through the cell is captured indirectly by the means of a voltmeter and its relationship with the resistor R_i . The current through the cell is measured and the results are logged. Here CA is a standard control amplifier while CF is configured as a current follower [1, p. 36].	5
1.4. A simple AC Bridge circuit: where $u(t)$ is the AC input perturbation, R_1 and R_2 are arbitrary resistors, <i>Cell</i> is the electrochemical cell with impedance Z_c , R_v is a variable resistor, C_v is a variable capacitor, and <i>Detector</i> is a device that detects when the voltage $v(t)$ is null.	8
1.5. Randles equivalent circuit model.	10
1.6. Nyquist plot of impedance with linear and semicircular extrapolation for a Randles cell with $R_s = 50$, $R_p = 250$, $C_{dl} = 2.5 \cdot 10^{-3}$, and $\sigma = 50$	16
1.7. Nyquist plot of impedance with linear and semicircular extrapolation for a Randles cell with $R_s = 50$, $R_p = 250$, $C_{dl} = 80 \cdot 10^{-6}$, and $\sigma = 15$	16
2.1. Block diagram for a generalized state-space representation.	20
2.2. Normalized error for model 1 (system order $m = 17$).	28
2.3. Normalized error for model 2 (system order $m = 17$).	28
2.4. Normalized error for model 3 (system order $m = 17$).	29
2.5. Normalized error for model 4 (system order $m = 17$).	29
2.6. Nyquist plot for model 1 (system order $m = 17$).	31
2.7. Nyquist plot for model 2 (system order $m = 17$).	31
2.8. Nyquist plot for model 3 (system order $m = 17$).	32
2.9. Nyquist plot for model 4 (system order $m = 17$).	32
3.1. Pole/zero plot in the s -domain for model 1 (system order $m = 17$).	34

3.2. Pole/zero plot in the s -domain for model 2 (system order $m = 17$).	34
3.3. Pole/zero plot in the s -domain for model 3 (system order $m = 17$).	35
3.4. Pole/zero plot in the s -domain for model 4 (system order $m = 17$).	35
3.5. Pole/zero plot in the z -domain for model 1 (system order $m = 17$).	37
3.6. Magnified pole/zero plot in the z -domain for model 1 (system order $m = 17$).	37
3.7. Magnified pole/zero plot in the z -domain for model 2 (system order $m = 17$).	38
3.8. Magnified pole/zero plot in the z -domain for model 3 (system order $m = 17$).	38
3.9. Magnified pole/zero plot in the z -domain for model 4 (system order $m = 17$).	39
3.10. Magnified pole/zero plot of implementation 1 (system order $m = 1$).	41
3.11. Frequency response of implementation 1 (system order $m = 1$) compared to the theoretical response.	42
3.12. Magnified pole/zero plot of implementation 2 (system order $m = 13$).	42
3.13. Frequency response of implementation 2 (system order $m = 13$) compared to the theoretical response.	43
3.14. Magnified pole/zero plot of implementation 3 (system order $m = 17$).	43
3.15. Frequency response of implementation 3 (system order $m = 17$) compared to the theoretical response.	44

LIST OF APPENDIX CODE-LISTINGS

<u>Listing</u>	<u>Page</u>
A.1. Mathematica symbolic simplification script. Confirms non-commutative simplification of Randles cell state-space relations. Utilizes the Non-Commutative Algebra and Gröbner Basis packages.	51
A.2. MATLAB script for constructing a state-space approximation of a CPE using the method described by Valsa et al. [2].	52
A.3. Script in MATLAB for comparing the continuous-time state-space model to the theoretical ideal.	55
A.4. Discretization MATLAB script which takes s -domain poles/zeros and overall gain and maps them to the z -domain by means of the matched z transform.	55
A.5. Script in MATLAB to pair poles/zeros and distribute gains evenly across subfilters. . .	56
A.6. Script in MATLAB for analyze the effects of fixed-point approximations to the discretized model.	60

1. BACKGROUND

1.1. Electrochemical Techniques

An *electrochemical process* is characterized by the presence of chemical reactions where changes in the number of valence electrons occur in at least one chemical species [3, p. 9], [4, pp. 1-2]. An *electrochemical cell* is an apparatus that facilitates electrochemical processes and consists of *electrodes* submerged in an electrolytic *test solution*. The most common setup involves three electrodes: a *working electrode*, a *counter* or *auxiliary electrode*, and a *reference electrode* [1, pp. 17-18], [5]. These cells facilitate the study of a variety of electrochemical reactions and is typically accomplished by observing and manipulating the voltage potential and current across pairs of electrodes. Electrochemical techniques have traditionally been used to study the rates of corrosion for different materials [5], the durability of coatings [3, p. 10], and the properties of fuel cells [6], but recent developments have found applications as a method of biosensing for lab-on-chip devices [7].

1.1.1. Electrochemical Techniques in the Study of Corrosion

While a thorough treatment of electrochemistry is beyond the scope of this thesis, this section presents a brief overview of the electrochemical process of *corrosion* and the ability of electrochemical techniques to ascertain a target material's *corrosion rate*. It is desirable to understand the kinetics of corrosion for different targets to aid in the development of corrosion-resistant materials and coatings. A simple yet powerful quantifier of a material's susceptibility to corrosion is a material's *penetration rate* [3, p. 13], typically measured in millimeters (of thickness) per year. Faraday's laws enable the determination of such indicators by relating electrical quantities, like *current density* (measured in mA/cm²), to mass changes [8, pp. 1-2], [3, p. 12].

Corrosion occurs when an *anode* and a *cathode* are connected by an electrolytic bridge that facilitates ionic and electrical conduction. The anodic and cathodic sites need not occur on different metals, as it is possible for both sites to occur along the surface on a single material [3, p. 11]. An archetypal example of corrosion would be the deterioration of a metallic surface coated with a thin film of atmospheric moisture [9]. For corrosion experiments conducted within an electrochemical cell: the target material is taken as the working electrode (WE), while the counter electrode (CE)

is taken to be another material that supports oxidation/reduction but does not itself undergo corrosion [10].

As a process, corrosion is characterized by two opposing chemical reactions, anodic *oxidation* and cathodic *species reduction* [3, p. 10]. As a result of Faraday's laws, the rate of each reaction has an associated current density. Since these reactions occur in opposition, the net current across the WE and CE is zero when the reactions occur in equilibrium [4, p. 381]. Therefore, it is not possible to directly determine the rate of corrosion through direct measurement of current between the WE and the CE at equilibrium. However, if the rates of the opposing reactions are adjusted, and current measurements are taken when the cell reaches a *steady-state*, the rates of the reactions at equilibrium can be inferred [5].

These rates are kept in balance by the potential of the target/WE. As a result, the reaction rates can be modified by manipulating this potential [9]. This requires an established reference voltage or ground; this is provided by a reference electrode (RE). A standard RE is a metal coated in salt [3, p. 22]. To maintain a constant potential across the interface, REs are typically fitted inside a glass/plastic housing (*Luggin capillary*) containing a separate electrolytic solution [4, p. 292]. This housing has a porous frit which facilitates ionic communication with the test solution [3, p. 22]. While the aforementioned RE configuration is typical of most electrochemical experiments, corrosion experiments forgo this setup in favor of a *pseudo-reference electrode* that consists of an additional sample of the target material submerged directly in the test solution [11].

A typical first step when analyzing a corrosion reaction is measuring the *equilibrium potential* between the WE and RE [5]. This potential is then manipulated to modify the rates of the underlying reactions. Voltages below the equilibrium potential cause the cathodic process to occur at a faster rate; voltages above the equilibrium potential cause the anodic process to occur at a faster rate. If current measurements are taken as the potential is varied (both above and below the equilibrium potential) and the electrochemical system has reached a steady-state, the data obtained can be extrapolated to estimate the *corrosion current density* at equilibrium which can then be used to determine the material's penetration rate via Faraday's laws [3, p. 44].

1.1.2. Tafel Extrapolation

A simple form of extrapolation called *Tafel extrapolation* calculates two linear regressions (*Tafel lines*) based on portions of a *polarization curve* and determines the location at which they

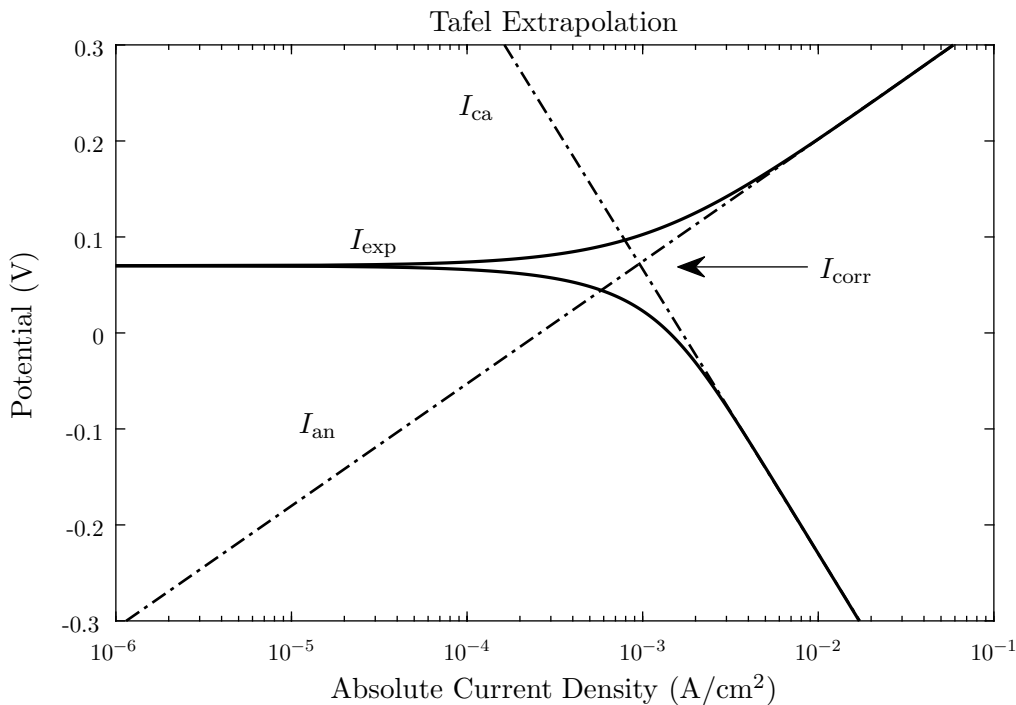


Figure 1.1. Tafel extrapolation of anodic and cathodic currents I_{an} and I_{ca} (Tafel lines), from experimental data I_{exp} , to determine corrosion current density at equilibrium I_{corr} .

intersect [9]. Polarization curves are semi-logarithmic plots of voltage applied with respect to current density I_{exp} (where current density is plotted on a logarithmic scale) [8, p. 215]. The linear portions of the curve, which occur at potentials further from equilibrium, are extrapolated (as theoretical anodic and cathodic currents I_{an} and I_{ca} respectively) toward equilibrium to determine the corrosion current density at equilibrium [3, p. 53], [9]. These linear regions are recommended to begin at least 50 to 100mV away from the equilibrium potential in either direction [3, p. 53]. This method is illustrated in Fig. 1.1, where the polarization curve for a theoretical cell is given along with Tafel lines and the estimated corrosion current density I_{corr} .

This method of extrapolation, while simple, is prone to issues in analysis. Many experimentally obtained polarization curves do not provide sufficient linear regions to support a proper regression [3, p. 55]. Furthermore, Tafel extrapolation presumes that dissolution occurs uniformly across the target's surface [3, p. 53]. Improper application of this method to a cell where dissolution does not occur uniformly can lead to erroneous conclusions.

While limited in scope, this overview of electrochemical techniques (as they relate to corrosion) exemplifies the methodology of *polarography*: estimating chemical properties (in this case

corrosion rate) from voltage/current relationships. Other techniques, such as the AC/periodic techniques rely on this same underlying principle.

1.2. The AC Impedance Method

AC or periodic electrochemical techniques are the defining methodology of *Electrochemical Impedance Spectroscopy* (EIS). Here the voltage/current relationships of polarography are presented in the form of impedance, the complex ratio of voltage over current. These techniques typically utilize the three-electrode setup described in Sec. 1.1. As with extrapolation of polarization curves, impedance data is used to infer information about the underlying electrochemical reactions.

1.2.1. Galvanostatic Interface

There are two approaches to perturbing and observing an electrochemical cell. The first approach leverages a *galvanostat*: a circuit that applies the input signal (perturbation) as the current between the WE and the CE and measures the output signal (observation) as the potential between the WE and the RE. The basic configuration of a galvanostat is given in Fig. 1.2.

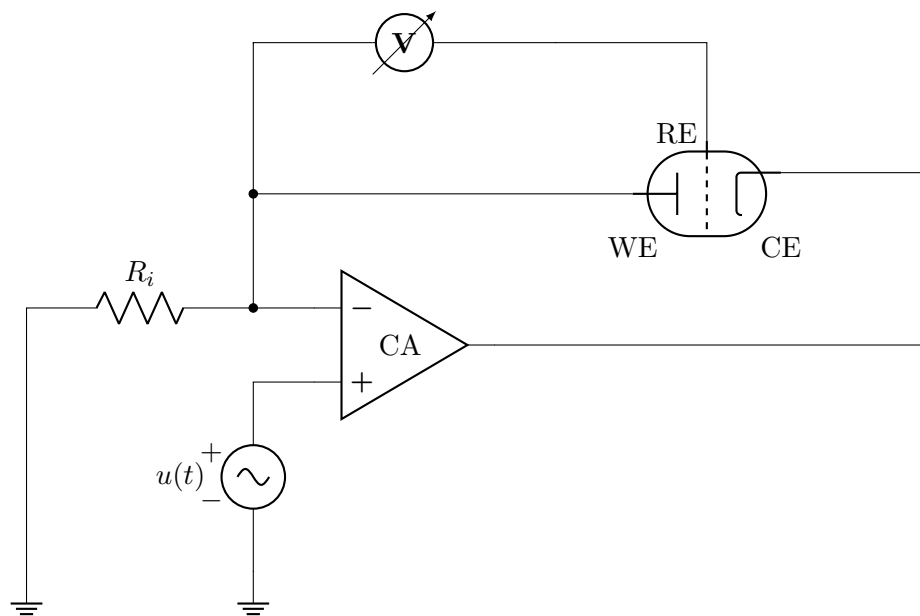


Figure 1.2. Basic configuration of a galvanostat. Here, current is controlled indirectly by the voltage source $u(t)$ which affects the current through the cell by means of its relationship with resistor R_i . The voltage across the cell is measured with a voltmeter and the results are logged [1, p. 38].

1.2.2. Potentiostatic Interface

The second, and more common approach, utilizes a *potentiostat*: a circuit that applies the input signal as the potential between the WE and the CE and measures the output signal as the current between the WE and RE. This was the approach used in the corrosion example given in Sec. 1.1. The basic configuration of a galvanostat is given in Fig. 1.3.

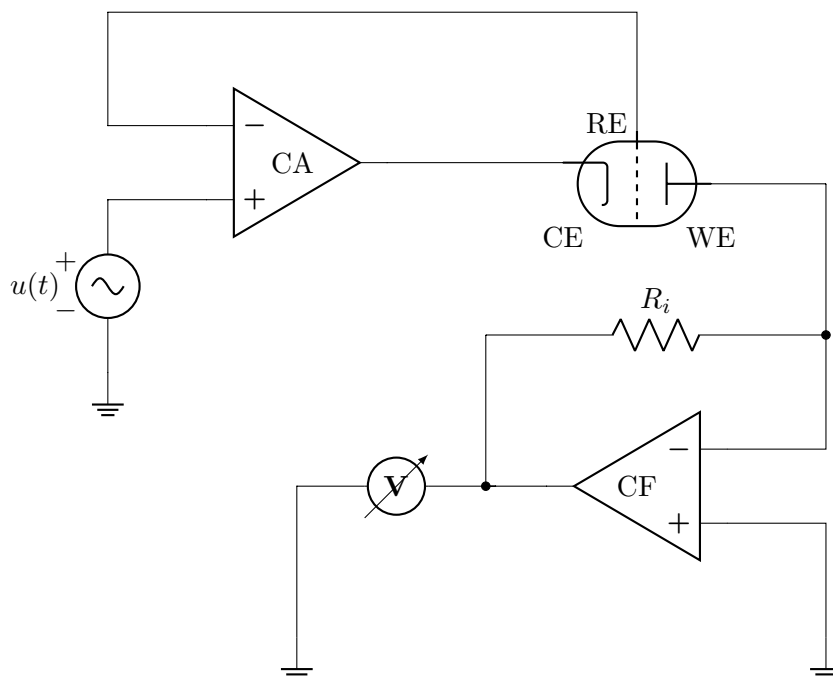


Figure 1.3. The basic configuration of a potentiostat. Here, voltage is controlled by the voltage source $u(t)$. The current through the cell is captured indirectly by the means of a voltmeter and its relationship with the resistor R_i . The current through the cell is measured and the results are logged. Here CA is a standard control amplifier while CF is configured as a current follower [1, p. 36].

While equipment that uses the galvanostatic approach tends to be simpler, the potentiostatic approach enjoys more popularity due to the increased importance of critical potentials over critical current densities for many experimental setups [3, p. 121]. Therefore, this approach is favored in this thesis; unless otherwise specified, the *input* to a cell should be taken to be the potential between the WE and the CE, and the *output* from a cell should be taken to be the current between the WE and RE.

In EIS, the electrochemical cell is perturbed by a sinusoidal (AC) signal with amplitude a_1 , phase θ_1 and radial frequency ω . For a *linear, time-invariant* (LTI) system H , the following relationship holds:

$$a_1 \cos(\omega t + \theta_1) \xrightarrow{H} a_2 \cos(\omega t + \theta_2). \quad (1.1)$$

where a_2 and θ_2 are the amplitude and phase (respectively) of the output signal. In other words, a sinusoidal input with a given frequency ω applied to an LTI system H will produce an output which is a scaled and phase shifted sinusoid of the same frequency.

For the LTI system given in Eq. (1.1), when the input is taken as the potential across a target load and the output is taken as the current across that same load (similar to inputs/outputs of an electrochemical cell), the impedance of the load Z_L at ω is

$$Z_L = \frac{a_1}{a_2} e^{j(\theta_1 - \theta_2)}. \quad (1.2)$$

Unfortunately, the input/output relationships of electrochemical cells are not truly linear or completely time-invariant. While the responses of electrochemical cells may tend toward a time-invariant steady-state after transients attenuate, input sinusoids generally result in the presence of *harmonics* in the output [12], [5]. Fortunately it can be shown that [1, p.237], for reversible reactions where the peak-to-peak voltage of the input signal is less than 10mV, all harmonics beyond the fundamental become negligible (i.e. the system behaves linearly). Once the perturbation signal has been applied and the cell has reached steady-state (transients have attenuated to negligible levels), measurements are taken to determine the impedance at ω .

The process of collecting impedance data can be time consuming, with some experiments taking many hours to collect a sufficient amount of data [5]. This is a result of the generally long duration of transients for most experiments. Unexpected reactions and changes in temperature can prevent the system from achieving steady state. When these factors are controlled for reversible charge transfer reactions, Bernzins and Delahay [13] have determined transients become negligible when

$$(\omega t)^{1/2} \gg 1, \quad (1.3)$$

where t is the time elapsed since the beginning of the experiment, and ω is the radial frequency of the input sinusoid. There are several experimental methods for obtaining impedance data. For each method described, it is assumed that impedance measurements for a given frequency are taken once the cell has reached steady-state.

1.2.3. Lissajous Figures

The most straightforward method for obtaining impedance data, the *direct method*, calculates impedance from the voltage/current relationship obtained via a Lissajous figure. Since the process of plotting Lissajous figures is agnostic with respect to which signal is considered to be the input/output, this method can be leveraged by both potentiostatic and galvanostatic approaches. When a potentiostatic setup with a fast rise time ($< 0.1\mu\text{s}$) [14, p. 11] is used, the direct method is capable of investigating the impedance response for frequencies up to 5kHz [1, p. 235].

1.2.4. AC Bridge

A slightly more complex experimental method utilizes an *AC bridge* circuit [1, pp. 230-233], [14, p. 9]. The AC bridge method applies a current (similar to a galvanostat) and calibrates a variable resistor and capacitor based off the readings of a detector in order to *balance* (alternatively *null*) the bridge. Once the bridge is balanced, the impedance of the cell can be determined by the calibration values of the variable resistor and capacitor.

The basic configuration of an AC bridge is depicted in Fig. 1.4. Here R_v and C_v are a resistor and capacitor with configurable resistance and capacitance (respectively) whose series impedance Z_v is

$$Z_v = R_v + \frac{1}{j\omega C_v}. \quad (1.4)$$

When the bridge is balanced, the following relationship holds:

$$\frac{Z_c}{R_1} = \frac{Z_v}{R_2}, \quad (1.5)$$

where Z_c is the impedance of the electrochemical cell. Substituting Eq. (1.4) into Eq. (1.5) and solving for the cell impedance Z_c yields

$$Z_c = \frac{R_1 R_v}{R_2 + R_1/(j\omega R_2 C_v)}. \quad (1.6)$$

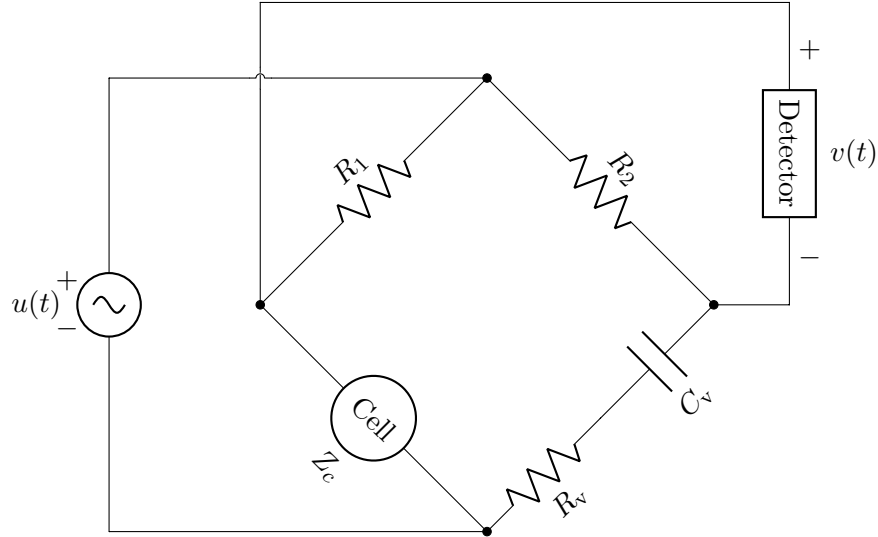


Figure 1.4. A simple AC Bridge circuit: where $u(t)$ is the AC input perturbation, R_1 and R_2 are arbitrary resistors, *Cell* is the electrochemical cell with impedance Z_c , R_v is a variable resistor, C_v is a variable capacitor, and *Detector* is a device that detects when the voltage $v(t)$ is null.

For a simple AC bridge configuration, impedance readings for frequencies between 0.2-2kHz are achievable. This frequency ceiling can be extended to 10kHz for bridge designs that incorporate *Wagner earthing* and up to 0.5MkHz for designs with a transformer ratio arm bridge [1, p. 233].

1.2.5. Phase Sensitive Detection

The *phase sensitive detection* method uses a *phase sensitive detector* (PSD) which measures the ratio of the amplitudes r and difference between phases ξ of two sinusoids

$$f(t) = a_1 \cos(\omega t + \theta_1) \quad (1.7)$$

$$\text{and } g(t) = a_2 \cos(\omega t + \theta_2) \quad (1.8)$$

as such

$$r = \frac{a_1}{a_2} \quad (1.9)$$

$$\text{and } \xi = \theta_1 - \theta_2. \quad (1.10)$$

When $f(t)$ is given to be the cell voltage and $g(t)$ is given to be the current across the cell, then r and ξ will be the magnitude and phase (respectively) of the impedance. This method accommodates impedance measurements for frequencies between 0.1Hz-5kHz [1, p. 234].

Modern EIS instruments such as *Gamry Instruments' Reference 600+* incorporate microprocessors which report measurements to software running on digital computers, feature multiple modes of operation (both galvanostatic and potentiostatic), and provide configurable feedback compensation to reduce unwanted voltage caused by the solution resistance between the WE and the CE [15, pp. 9-10]. Once the impedance measurements have been captured across the range of available frequencies, the data is fit to the impedance of a theoretical circuit model that has component values which correspond to electrochemical properties.

1.3. Randles Equivalent Circuit

For quasi-reversible reactions, the voltage/current relationships between the WE and RE, and the WE and the CE (respectively) can be modeled by an equivalent electrical circuit known as a *Randles circuit* (or *Randles cell*). The resistance/capacitance/strength of each component in a Randles cell is indicative of various electrochemical properties. The Randles circuit in Fig. 1.5 with input voltage $u(t)$ and measured current $i_T(t)$, consists of following components:

- An initial resistor R_s models the resistivity of the electrolytic solution.
- A capacitor C_{dl} models the double layer capacitance that forms between the WE and the solution [1].
- A resistor R_p models the *polarization resistivity*. The polarization resistivity gives the potential/current relationship of the cell as it undergoes polarization (see Tafel lines in Sec. 1.1). This value is related to the *charge transfer rate constant* [1, p. 267] and is inversely related to the corrosion current density in corrosion testing [3, p. 134].
- A Warburg Element \mathcal{W} is a theoretical component that models the diffusion process (which does not depend on the charge transfer rate[1]). Warburg elements have an associated *Warburg coefficient* σ , which is related to the diffusion coefficients of the underlying process [5].

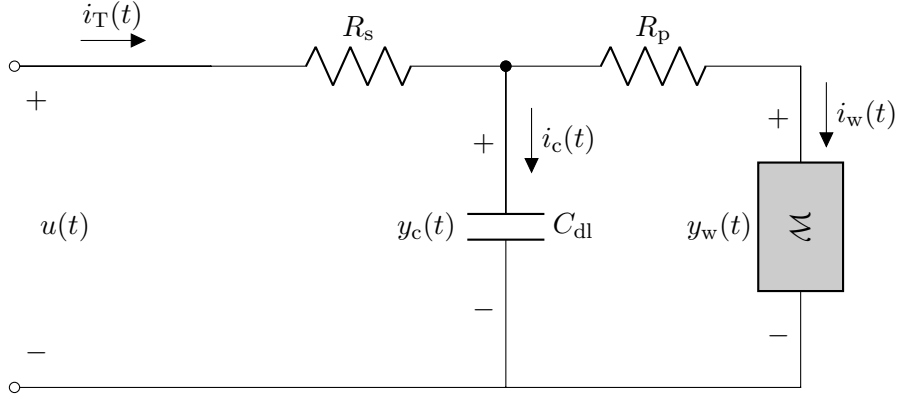


Figure 1.5. Randles equivalent circuit model.

Given a diffusion layer of infinite thickness, the impedance of a Warburg element Z_W is defined as

$$Z_W(\omega) = \sigma\omega^{-1/2}(1 - j). \quad (1.11)$$

The total theoretical impedance Z_{th} for a Randles cell can be calculated as

$$Z_{th}(\omega) = R_s + \frac{1}{C_{dl}j\omega + \frac{1}{R_p + Z_W(\omega)}}. \quad (1.12)$$

A complete derivation of each component value with respect to the underlying electrochemical processes and quantities is beyond the scope of this thesis, however, a detailed presentation of such a derivation is given by D. McDonald [1].

1.4. Nyquist Plots of Cell Impedance

Given an arbitrary electrochemical cell that is suitably modeled by a Randles cell, the impedance response of the cell can be plotted parametrically (with respect to ω) along the real and imaginary axes. Such a plot is called a *Nyquist plot* of impedance. Because cells that are suitably modeled by a Randles circuit typically exhibit capacitive behavior, the imaginary component of the impedance data is usually negative. Therefore, it is convenient to invert the imaginary axis such that the curve is displayed in the upper quadrants of the graph.

Let $x_{\text{nyq}}(\omega)$ and $y_{\text{nyq}}(\omega)$ be parametric functions of ω , than a Nyquist plot of a generalized Randles cell with an impedance $Z_{\text{th}}(\omega)$ given by Eq. (1.12) would imply

$$x_{\text{nyq}}(\omega) = \text{Re}\{Z_{\text{th}}(\omega)\} \quad (1.13)$$

$$\text{and } y_{\text{nyq}}(\omega) = -\text{Im}\{Z_{\text{th}}(\omega)\}. \quad (1.14)$$

To simplify future expressions, let the intermediate function $g_{\text{nyq}}(\omega)$ be given as

$$g_{\text{nyq}}(\omega) = \sigma\omega^{-1/2}. \quad (1.15)$$

With this definition of $g_{\text{nyq}}(\omega)$, the equation for the impedance of a Warburg element $Z_{\text{W}}(\omega)$ from Eq. (1.11) can be written as

$$Z_{\text{W}}(\omega) = (1 - j)g_{\text{nyq}}(\omega). \quad (1.16)$$

Substituting this definition of $Z_{\text{W}}(\omega)$ into the impedance of a generalized Randles cell $Z_{\text{th}}(\omega)$ given by Eq. (1.12) yields

$$Z_{\text{th}}(\omega) = R_{\text{s}} + \frac{1}{C_{\text{dl}}j\omega + \frac{1}{R_{\text{p}} + (1-j)g_{\text{nyq}}(\omega)}}. \quad (1.17)$$

In order to obtain closed-form solutions for $x_{\text{nyq}}(\omega)$ and $y_{\text{nyq}}(\omega)$ it is necessary to obtain the real and imaginary components of $Z_{\text{th}}(\omega)$. This requires that the fractional from Eq. (1.17) term be broken up. Note that the addition in the denominator of the fraction can be rewritten as

$$C_{\text{dl}}j\omega + \frac{1}{R_{\text{p}} + (1-j)g_{\text{nyq}}(\omega)} \implies \frac{1 + C_{\text{dl}}\omega g_{\text{nyq}}(\omega) + jC_{\text{dl}}\omega(R_{\text{p}} + g_{\text{nyq}}(\omega))}{R_{\text{p}} + (1-j)g_{\text{nyq}}(\omega)}. \quad (1.18)$$

Considering the preceding expression occurs in Eq. (1.17) within the denominator of a fraction whose numerator is unity, the fraction in the preceding expression will become flipped as

$$\implies \frac{R_{\text{p}} + (1-j)g_{\text{nyq}}(\omega)}{1 + C_{\text{dl}}\omega g_{\text{nyq}}(\omega) + jC_{\text{dl}}\omega(R_{\text{p}} + g_{\text{nyq}}(\omega))}. \quad (1.19)$$

The complex character of the denominator in this new expression can be eliminated by multiplying the numerator and denominator by the *complex-conjugate* of the denominator

$$\implies \frac{R_p + (1-j)g_{\text{nyq}}(\omega)}{1 + C_{\text{dl}}\omega g_{\text{nyq}}(\omega) + jC_{\text{dl}}\omega(R_p + g_{\text{nyq}}(\omega))} \left[\frac{1 + C_{\text{dl}}\omega g_{\text{nyq}}(\omega) - jC_{\text{dl}}\omega(g_{\text{nyq}}(\omega) + R_p)}{1 + C_{\text{dl}}\omega g_{\text{nyq}}(\omega) - jC_{\text{dl}}\omega(g_{\text{nyq}}(\omega) + R_p)} \right], \quad (1.20)$$

which yields

$$\implies \frac{R_p + g_{\text{nyq}}(\omega) - j[g_{\text{nyq}}(\omega) + C_{\text{dl}}\omega(2a^2(\omega) + 2R_p g_{\text{nyq}}(\omega) + R_p^2)]}{(1 + C_{\text{dl}}\omega g_{\text{nyq}}(\omega))^2 + C_{\text{dl}}^2\omega^2(g_{\text{nyq}}(\omega) + R_p)^2}. \quad (1.21)$$

Applying the definition of $g_{\text{nyq}}(\omega)$ from Eq. (1.15) and rewriting the fractional portion of Eq. (1.17) as Eq. (1.21) gives an alternate form for the impedance across a Randles cell as

$$Z_{\text{th}}(\omega) = R_s + \frac{R_p + \sigma\omega^{-1/2} - j[\sigma\omega^{-1/2} + C_{\text{dl}}(2\sigma^2 + 2R_p\sigma\omega^{1/2} + R_p^2\omega)]}{(1 + C_{\text{dl}}\sigma\omega^{1/2})^2 + C_{\text{dl}}^2\omega^2(\sigma\omega^{-1/2} + R_p)^2}. \quad (1.22)$$

This reformulation of $Z_{\text{th}}(\omega)$ allows for the real and imaginary portions of the expression to be easily extracted. Recalling the definitions from Eqs. (1.13) and (1.14), the closed-form expressions of $x_{\text{nyq}}(\omega)$ and $y_{\text{nyq}}(\omega)$ are

$$x_{\text{nyq}}(\omega) = R_s + \frac{R_p + \sigma\omega^{-1/2}}{(1 + C_{\text{dl}}\sigma\omega^{1/2})^2 + C_{\text{dl}}^2\omega^2(\sigma\omega^{-1/2} + R_p)^2} \quad (1.23)$$

$$\text{and } y_{\text{nyq}}(\omega) = \frac{\sigma\omega^{-1/2} + C_{\text{dl}}(2\sigma^2 + 2R_p\sigma\omega^{1/2} + R_p^2\omega)}{(1 + C_{\text{dl}}\sigma\omega^{1/2})^2 + C_{\text{dl}}^2\omega^2(\sigma\omega^{-1/2} + R_p)^2}. \quad (1.24)$$

To best understand the character of this family of parametric curves, it is desirable to understand the behavior of $x_{\text{nyq}}(\omega)$ and $y_{\text{nyq}}(\omega)$ at the extremities of ω : when $\omega \rightarrow 0$ and $\omega \rightarrow \infty$. This behavior is dictated by the lowest/highest powers of ω in the numerators and denominators of $x_{\text{nyq}}(\omega)$ and $y_{\text{nyq}}(\omega)$. To aid in this analysis Eqs. (1.23) and (1.24) are expanded with respect to ω as

$$x_{\text{nyq}}(\omega) = R_s + \frac{R_p + \sigma\omega^{-1/2}}{1 + 2C_{\text{dl}}\sigma\omega^{1/2} + 2C_{\text{dl}}\sigma^2\omega + 2C_{\text{dl}}^2R_p\sigma\omega^{3/2} + C_{\text{dl}}^2R_p^2\omega^2} \quad (1.25)$$

$$\text{and } y_{\text{nyq}}(\omega) = \frac{\sigma\omega^{-1/2} + 2C_{\text{dl}}\sigma^2 + 2C_{\text{dl}}R_p\sigma\omega^{1/2} + C_{\text{dl}}R_p^2\omega}{1 + 2C_{\text{dl}}\sigma\omega^{1/2} + 2C_{\text{dl}}\sigma^2\omega + 2C_{\text{dl}}^2R_p\sigma\omega^{3/2} + C_{\text{dl}}^2R_p^2\omega^2}. \quad (1.26)$$

1.4.1. Behavior as ω Approaches Zero

For the case in which $\omega \rightarrow 0$, the $\sigma\omega^{-1/2}$ term dominates the numerator of $x_{\text{nyq}}(\omega)$ while its denominator tends toward unity. This results in

$$x_{\text{nyq}}(\omega) = R_s + R_p + \sigma\omega^{-1/2}. \quad (1.27)$$

In a similar manner, for $y_{\text{nyq}}(\omega)$ as $\omega \rightarrow 0$: the $\sigma\omega^{-1/2}$ term dominates and the $2C_{\text{dl}}\sigma^2$ term remains in the numerator while the denominators tends toward unity. This yields

$$y_{\text{nyq}}(\omega) = 2C_{\text{dl}}\sigma^2 + \sigma\omega^{-1/2}. \quad (1.28)$$

In order to ascertain the relationship between $x_{\text{nyq}}(\omega)$ and $y_{\text{nyq}}(\omega)$ for $\omega \rightarrow 0$, ω can be eliminated from Eqs. (1.27) and (1.28) by solving Eq. (1.27) for $\omega^{-1/2}$, resulting in

$$\omega^{-1/2} = \frac{x_{\text{nyq}}(\omega) - R_s - R_p}{\sigma}. \quad (1.29)$$

Finally, substituting Eq. (1.29) into Eq. (1.28) yields

$$y_{\text{nyq}}(\omega) = x_{\text{nyq}}(\omega) + 2C_{\text{dl}}\sigma^2 - R_s - R_p. \quad (1.30)$$

This relationship in Eq. (1.30) of $y_{\text{nyq}}(\omega)$ with respect to $x_{\text{nyq}}(\omega)$ describes a line with a slope of unity and a x -intercept of $2C_{\text{dl}}\sigma^2 - R_s - R_p$.

1.4.2. Behavior as ω Approaches Infinity

For the case in which $\omega \rightarrow \infty$, the $C_{\text{dl}}^2 R_p^2 \omega^2$ term dominates the denominator (while still being offset by +1) of $x_{\text{nyq}}(\omega)$ from Eq. (1.25) while its numerator tends toward R_p . This results in

$$x_{\text{nyq}}(\omega) = R_s + \frac{R_p}{1 + C_{\text{dl}}^2 R_p^2 \omega^2}. \quad (1.31)$$

In a similar manner, for $y_{\text{nyq}}(\omega)$ as $\omega \rightarrow \infty$: the $C_{\text{dl}}^2 R_{\text{p}}^2 \omega^2$ term dominates the denominator (while still being offset by +1) while the $C_{\text{dl}} R_{\text{p}}^2 \omega$ term dominates the numerator. This gives

$$y_{\text{nyq}}(\omega) = \frac{C_{\text{dl}} R_{\text{p}}^2 \omega}{1 + C_{\text{dl}}^2 R_{\text{p}}^2 \omega^2}. \quad (1.32)$$

It is desirable to eliminate ω from Eqs. (1.31) and (1.32) in order to ascertain the relationship between $x_{\text{nyq}}(\omega)$ and $y_{\text{nyq}}(\omega)$ for $\omega \rightarrow \infty$. Solving Eq. (1.31) for ω^2 gives

$$\omega^2 = \frac{1}{C_{\text{dl}}^2 R_{\text{p}}^2} \left(\frac{R_{\text{p}}}{x_{\text{nyq}}(\omega) - R_{\text{s}}} - 1 \right). \quad (1.33)$$

Substituting the instance of ω^2 in Eq. (1.32) with the result from Eq. (1.33) yields

$$y_{\text{nyq}}(\omega) = \frac{C_{\text{dl}} R_{\text{p}}^2 \omega}{1 + \frac{R_{\text{p}}}{x_{\text{nyq}}(\omega) - R_{\text{s}}} - 1} = C_{\text{dl}} R_{\text{p}} (x_{\text{nyq}}(\omega) - R_{\text{s}}) \omega. \quad (1.34)$$

The result of Eq. (1.34) is squared in order to obtain another instance of ω^2 for substitution. This gives

$$y_{\text{nyq}}^2(\omega) = C_{\text{dl}}^2 R_{\text{p}}^2 (x_{\text{nyq}} - R_{\text{s}})^2 \omega^2. \quad (1.35)$$

Substituting ω^2 from Eq. (1.32) results in

$$y_{\text{nyq}}^2(\omega) = (x_{\text{nyq}}(\omega) - R_{\text{s}})^2 \left(\frac{R_{\text{p}}}{x_{\text{nyq}}(\omega) - R_{\text{s}}} - 1 \right). \quad (1.36)$$

Bringing every term over to the left-hand-side and expanding/distributing yields

$$y_{\text{nyq}}^2(\omega) + x_{\text{nyq}}^2(\omega) - (2R_{\text{s}} + R_{\text{p}})x_{\text{nyq}}(\omega) + R_{\text{p}}R_{\text{s}} + R_{\text{s}}^2 = 0. \quad (1.37)$$

Completing the square with respect to $x_{\text{nyq}}(\omega)$ gives

$$y_{\text{nyq}}^2(\omega) + \left(x_{\text{nyq}}(\omega) - \frac{2R_{\text{s}} + R_{\text{p}}}{2} \right)^2 - \left(\frac{2R_{\text{s}} + R_{\text{p}}}{2} \right)^2 + R_{\text{p}}R_{\text{s}} + R_{\text{s}}^2 = 0. \quad (1.38)$$

Finally Eq. (1.38) simplifies to

$$y_{\text{nyq}}^2(\omega) + \left(x_{\text{nyq}}(\omega) - R_s - \frac{R_p}{2} \right)^2 = \frac{R_p^2}{4}. \quad (1.39)$$

This relationship in Eq. (1.39) of $y_{\text{nyq}}(\omega)$ with respect to $x_{\text{nyq}}(\omega)$ describes a circle centered at $(R_s + R_p/2, 0)$ with a radius of $R_p/2$.

1.4.3. Analysis of Nyquist Plots

Inferences about the component values in a Randles cell (i.e. R_s , R_p , C_{dl} , and σ) can be made by analyzing the Nyquist plot of a cell's impedance data. From Eq. (1.27), it is known that $x_{\text{nyq}}(\omega)$ grows when $\omega \rightarrow 0$; therefore, the Nyquist plot of a generalized Randles cell will tend toward a 45° line which travels up and to the right, as $\omega \rightarrow 0$. This linear portion of the curve can be extrapolated to intersect the real-axis [1, 268]. From Eq. (1.30), the point of this intersection can be used to determine the value of $2C_{\text{dl}}\sigma^2 - R_s - R_p$. This process of linear extrapolation in a Nyquist plot is depicted in Fig. 1.6. If the values of either C_{dl} or σ are particularly small, the $2C_{\text{dl}}\sigma^2$ term in the x -intercept becomes negligible; this results in the x -intercept occurring roughly at $R_s + R_p$ as depicted in Fig. 1.7.

Consider the upper semicircle from the relation in Eq. (1.39). This is the most prominent feature as $\omega \rightarrow \infty$. This semicircle is centered at $(R_s + R_p/2, 0)$ with a radius of $R_p/2$ (and a diameter of R_p). It intersects the real axis at R_s on the left side and $R_s + R_p$ on the right. From Eqs. (1.31) and (1.32) it can be seen that the limits as $\lim_{\omega \rightarrow \infty}$, for $x_{\text{nyq}}(\omega)$ and $y_{\text{nyq}}(\omega)$ are R_s and zero respectively. This suggests that as $\omega \rightarrow \infty$, the Nyquist curve will more closely follow the upper semicircle inferred from Eq. (1.39) from right to left, asymptotically approaching the point $(R_s, 0)$. These properties of the semicircle enable the derivation of the values R_s and R_p through extrapolation. This method of extrapolating semicircles and is depicted in Figs. 1.6 and 1.7.

While Nyquist plots provide graphical insight into the underlying component values of an electrochemical cell's equivalent circuit, modern software uses other, more advanced, techniques (least-squares fitting techniques) for determining these values from impedance data [5].

1.5. Warburg Element

The component of most interest in a Randles circuit is the Warburg element, which is defined by the impedance relationship given by Eq. (1.11), where ω is the radial frequency and σ

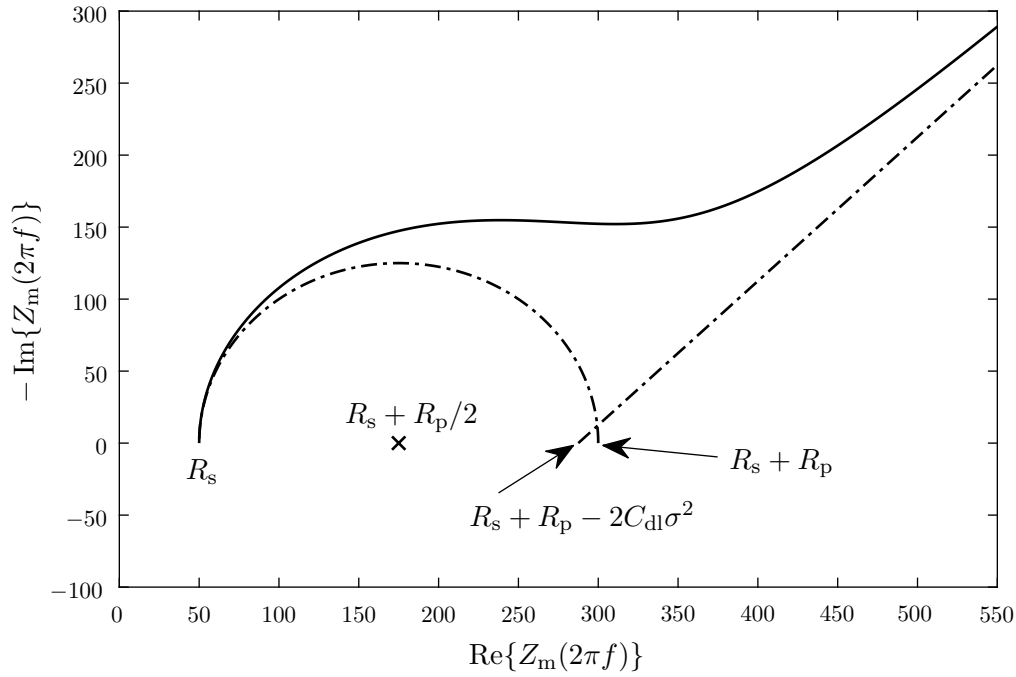


Figure 1.6. Nyquist plot of impedance with linear and semicircular extrapolation for a Randles cell with $R_s = 50$, $R_p = 250$, $C_{dl} = 2.5 \cdot 10^{-3}$, and $\sigma = 50$.

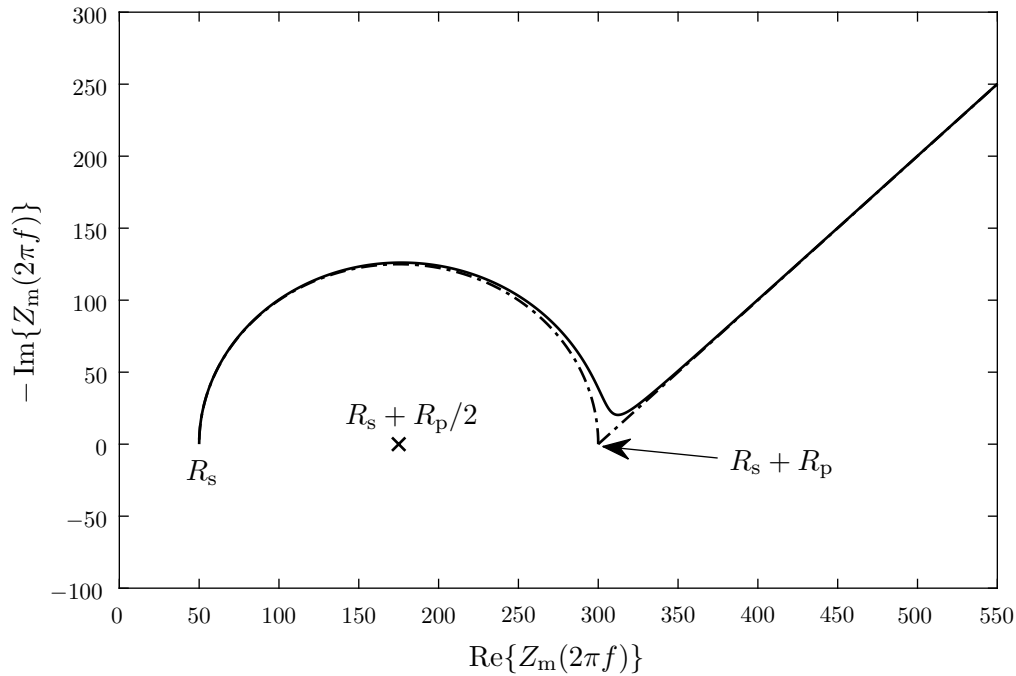


Figure 1.7. Nyquist plot of impedance with linear and semicircular extrapolation for a Randles cell with $R_s = 50$, $R_p = 250$, $C_{dl} = 80 \cdot 10^{-6}$, and $\sigma = 15$.

is the *Warburg coefficient*. The Warburg element is a theoretical circuit element with no analogous physical component.

Warburg elements are a subset of the more general class of components known as *constant phase elements* (CPEs). CPEs have the impedance relationship

$$Z_{\text{CPE}}(\omega) = D_s(j\omega)^{-a} \quad (1.40)$$

for $D_s \in (0, \infty)$ and $a \in [0, 1]$,

where D_s is the gain of the CPE and a is related to the phase offset ϕ by the relationship

$$\phi = a\frac{\pi}{2}. \quad (1.41)$$

Note that capacitors are a subset of CPEs. The impedance relationship for a capacitor with capacitance C

$$Z_C(\omega) = \frac{1}{Cj\omega} \quad (1.42)$$

can be derived from Eq. (1.40) by taking $a = 1$ and $D_s = 1/C$.

In like manner, the impedance relationship for a Warburg element from Eq. (1.11) can be derived from Eq. (1.40) by taking $a = 1/2$ and $D_s = \sqrt{2}\sigma$.

Note that while a capacitor is a CPE which can be realized by a traditional circuit component, a Warburg element has no such trivial realization. This is due to the non-integer value of a from Eq. (1.40) required for the element's impedance. Such non-integer values result in either fractional derivatives when determining a time-domain relationship or require a system with infinite memory [16].

Given the finite range of frequencies applied in EIS [5], it is not necessary to require a perfect realization of a Warburg element across all frequencies. Rather, a sufficient approximation of the element across the necessary frequencies proves suitable.

1.6. Approximating the Warburg Element over Frequencies of Interest

Valsa et al. [2] give a method to approximate the behavior of a CPE over frequencies of interest by means of a series of m parallel

$$\text{resistors: } \left\{ R_1, \dots, R_{m-1}, R_m \right\} \quad (1.43)$$

$$\text{and capacitors: } \left\{ C_1, \dots, C_{m-1}, C_m \right\} \quad (1.44)$$

preceded by an initial resistor R_0 in series with an initial capacitor C_0 . Since Warburg elements are a subset of CPEs, this configuration can be used to approximate a generalized Warburg element with a given Warburg coefficient σ . The total impedance of this configuration given in terms of its components is

$$\tilde{Z}_{\text{CPE}}(\omega) = R_0 + \frac{1}{C_0 j \omega} + \sum_{k=1}^m \frac{R_k}{1 + R_k C_k j \omega}. \quad (1.45)$$

The following procedure from Valsa et al. [2, pp. 622-623] determines the values of the resistors and capacitors. Given a constant phase offset ϕ ($\pi/4$ for a Warburg element from Eq. (1.41)), gain D_s ($\sqrt{2}\sigma$ for a Warburg element), max phase ripple Δ_ϕ , lower frequency bound ω_0 , and upper frequency bound ω_1 , ϵ and intermediate constant q [2, Eq. 20] are determined as

$$\epsilon = -\frac{2\phi}{\pi} \quad (1.46)$$

$$\text{and } q = \frac{0.24}{1 + \Delta_\phi \cdot 180/\pi}. \quad (1.47)$$

To achieve the resolution of accuracy specified by ω_0 , ω_1 and Δ_ϕ , the order of the RC series m is computed as

$$m = \left\lceil \frac{\ln \omega_0 - \ln \omega_1}{\ln q} \right\rceil. \quad (1.48)$$

The relationship of each consecutive resistor/capacitor in the chain of m RC filters is related in a geometric series. The first elements in each series are given to be

$$C_1 = 1 \quad (1.49)$$

$$\text{and} \quad R_1 = 1/\omega_0. \quad (1.50)$$

The remaining elements can be computed as

$$R_k = R_1 r_a^{k-1} \quad (1.51)$$

$$\text{and} \quad C_k = C_1 r_b^{k-1} \quad (1.52)$$

$$\text{for } k = \left\{ 1, \dots, m-1, m \right\},$$

where r_a and r_b are the geometric ratios

$$r_a = 10^{\epsilon \log_{10} q} \quad (1.53)$$

$$\text{and} \quad r_b = q/r_a. \quad (1.54)$$

The corrective initial resistance R_0 and capacitance C_0 are computed as

$$R_0 = R_1 \frac{r_a^m}{1 - r_a} \quad (1.55)$$

$$\text{and} \quad C_0 = C_1 \frac{1 - r_b}{r_b}. \quad (1.56)$$

In order to obtain the desired gain D_s , the final values of every resistor (see Eq. (1.43)) and capacitor (see Eq. (1.44)) are multiplied by the *gain correction factor* g given by

$$g = \frac{D_s}{|\tilde{Z}_{\text{CPE}}(\omega_{\text{avg}})|}, \quad (1.57)$$

$$\text{where} \quad \omega_{\text{avg}} = \left(\frac{r_a}{r_b} \right)^{1/4} \frac{1}{R_1 C_1 q^{\lceil m/2 - 1 \rceil}}. \quad (1.58)$$

2. MODELING A RANDLES CELL IN STATE-SPACE

State-space representations allow for a holistic model of a Randles cell which facilitates the derivation of a variety of analog and digital realizations. This thesis derives a set of state-space equations that model the potentiostatic interface (described in Sec. 1.2) to a Randles circuit using an approximation of a Warburg element (described in Sec. 1.6) [17]. A standard state-space representation [18, p. 58] is a set of first-order linear differential equations which relate a state-vector $\mathbf{x}(t)$ to input-vector $u(t)$ and output-vector $y(t)$ by means of the relations

$$\dot{\mathbf{x}}(t) = \mathbf{A}\mathbf{x}(t) + \mathbf{B}u(t) \quad (2.1)$$

$$\text{and } y(t) = \mathbf{C}\mathbf{x}(t) + \mathbf{D}u(t). \quad (2.2)$$

Note that the derivative $\dot{\mathbf{x}}(t)$ is taken with respect to time. A block diagram representation of these relations is given in Fig. 2.1. For this general set of state-space equations, the behavior of the system is informed by the matrices \mathbf{A} , \mathbf{B} , \mathbf{C} , and \mathbf{D} .

To determine the appropriate matrices \mathbf{A} , \mathbf{B} , \mathbf{C} , and \mathbf{D} that model the potentiostatic interface to a Randles cell, it is beneficial to derive state-space representations for the memory storing components within the cell: the capacitor C_{dl} and the approximation of a Warburg Element \mathcal{W} (see Fig. 1.5).

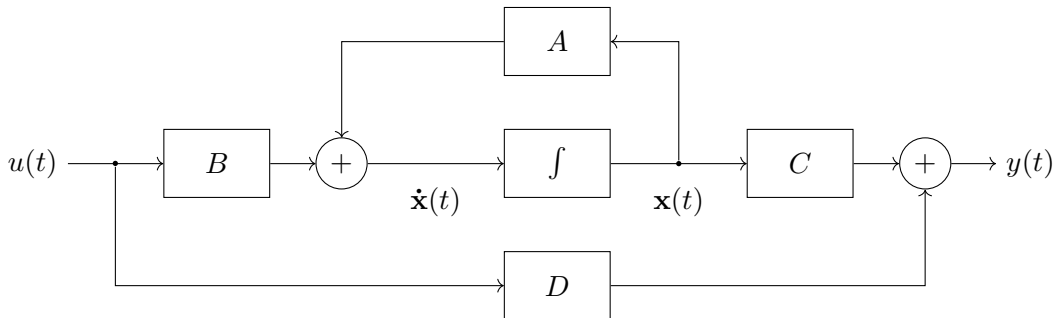


Figure 2.1. Block diagram for a generalized state-space representation.

To simplify notation going forward, inputs $u(t)$, outputs $y(t)$ and state-vectors $\mathbf{x}(t)$ of future state-space relations will omit the reference to the independent variable t (i.e. will become u , y and \mathbf{x}). This does not imply a loss of dependence on t , rather, each aforementioned value maintains this dependency despite it no longer being explicitly represented.

2.1. Capacitor in State-Space

Assume that y_c is the output of a state-space system that models the voltage across a capacitor with respect to the current i_c flowing into it (see Fig. 1.5), having the associated state-vector \mathbf{x}_c , matrices \mathbf{A}_c , \mathbf{B}_c , \mathbf{C}_c and scalar D_c which satisfy

$$\dot{\mathbf{x}}_c = \mathbf{A}_c \mathbf{x}_c + \mathbf{B}_c i_c \quad (2.3)$$

$$\text{and} \quad y_c = \mathbf{C}_c \mathbf{x}_c + D_c i_c. \quad (2.4)$$

Let C_{dl} be the capacitance of the capacitor in the Randles circuit. The values of \mathbf{A}_c , \mathbf{B}_c , \mathbf{C}_c and D_c which model such a capacitor are

$$\mathbf{A}_c = 0, \quad (2.5)$$

$$\mathbf{B}_c = 1, \quad (2.6)$$

$$\mathbf{C}_c = 1/C_{dl}, \quad (2.7)$$

$$\text{and} \quad D_c = 0. \quad (2.8)$$

2.2. Approximation of a Warburg Element in State-Space

Let $y_w(t)$ be the voltage across an approximation of a Warburg element from Sec. 1.6 where $\phi = \pi/4$ and $D_s = \sqrt{2}\sigma$, with free parameters Δ_ϕ , σ , ω_0 and ω_1 .

From Ohm's law, given a current through the Warburg element, $i_w(t)$, the voltage $y_w(t)$ should satisfy

$$Y_w(\omega) = \tilde{Z}_{CPE}(\omega) \cdot I_w(\omega), \quad (2.9)$$

where $I_w(\omega)$ and $Y_w(\omega)$ are the Fourier transforms of $i_w(t)$ and $y_w(t)$ respectively and $\tilde{Z}_{CPE}(\omega)$ is from Eq. (1.45). Notice that $\tilde{Z}_{CPE}(\omega)$ is the transfer function of a system with order $m + 1$

whose input is current i_w and output is voltage y_w (see Fig. 1.5). There exists some system of first order differential equations with state-vector \mathbf{x}_w , matrices \mathbf{A}_w , \mathbf{B}_w , \mathbf{C}_w and scalar D_w that satisfy Eq. (2.9) with the form

$$\dot{\mathbf{x}}_w = \mathbf{A}_w \mathbf{x}_w + \mathbf{B}_w i_w \quad (2.10)$$

$$\text{and} \quad y_w = \mathbf{C}_w \mathbf{x}_w + D_w i_w. \quad (2.11)$$

Since the transfer function of the system is known and $\tilde{Z}_{\text{CPE}}(\omega)$ from Eq. (1.45) is in *partial fraction expanded form*, the *Jordan canonical form* is employed to determine the values

$$\mathbf{A}_w = \begin{bmatrix} 0 & 0 & 0 & \dots & 0 & 0 \\ 0 & -\frac{1}{R_1 C_1} & 0 & \dots & 0 & 0 \\ 0 & 0 & -\frac{1}{R_2 C_2} & \dots & 0 & 0 \\ \vdots & \vdots & \vdots & \ddots & \vdots & \vdots \\ 0 & 0 & 0 & \dots & -\frac{1}{R_{m-1} C_{m-1}} & 0 \\ 0 & 0 & 0 & \dots & 0 & -\frac{1}{R_m C_m} \end{bmatrix}, \quad (2.12)$$

$$\mathbf{B}_w = \begin{bmatrix} 1 \\ 1 \\ 1 \\ \vdots \\ 1 \\ 1 \end{bmatrix}, \quad (2.13)$$

$$\mathbf{C}_w = \left[\frac{1}{C_0} \quad \frac{1}{C_1} \quad \frac{1}{C_2} \quad \dots \quad \frac{1}{C_{m-1}} \quad \frac{1}{C_m} \right], \quad (2.14)$$

$$\text{and} \quad D_w = R_0, \quad (2.15)$$

where

$$\text{resistances: } \left\{ R_0, R_1, \dots, R_{m-1}, R_m \right\} \quad (2.16)$$

$$\text{and capacitances: } \left\{ C_0, C_1, \dots, C_{m-1}, C_m \right\} \quad (2.17)$$

are calculated via the method detailed in Sec. 1.6.

2.3. Randles Cell in State-Space

Modeling a cell in a manner consistent with a potentiostatic setup requires the system's input to be a voltage potential and the system's output to be the total current through the cell. Let u be the input voltage potential, i_T be the total current through the cell, y_c be the voltage across the capacitor from Eq. (2.4), y_w be the voltage across the approximation of a Warburg element from Eq. (2.11), i_c be the current through the capacitor, i_w be the current through the Warburg element, R_p be the resistance in series with the Warburg element, and R_s be the resistor at the head of the circuit (see Fig. 1.5). From Kirchhoff's relations:

$$y_c = R_p i_w + y_w, \quad (2.18)$$

$$u = R_s (i_c + i_w) + y_c, \quad (2.19)$$

$$\text{and } i_T = i_c + i_w. \quad (2.20)$$

Solving for i_c and i_w with respect to y_c and y_w yields

$$i_c = \frac{1}{R_p R_s} (R_p u - R_p y_c - R_s y_c + R_s y_w) \quad (2.21)$$

$$\text{and } i_w = \frac{1}{R_p} (y_c - y_w). \quad (2.22)$$

Substituting Eqs. (2.21) and (2.22) into Eqs. (2.3), (2.4), (2.10), and (2.11) yields

$$\dot{\mathbf{x}}_c = \mathbf{A}_c \mathbf{x}_c + \mathbf{B}_c \frac{R_p(u - y_c) + R_s(y_w - y_c)}{R_p R_s}, \quad (2.23)$$

$$y_c = \mathbf{C}_c \mathbf{x}_c + D_c \frac{R_p(u - y_c) + R_s(y_w - y_c)}{R_p R_s}, \quad (2.24)$$

$$\dot{\mathbf{x}}_w = \mathbf{A}_w \mathbf{x}_w + \mathbf{B}_w \frac{y_c - y_w}{R_p}, \quad (2.25)$$

$$\text{and } y_w = \mathbf{C}_w \mathbf{x}_w + D_w \frac{y_c - y_w}{R_p}. \quad (2.26)$$

Solving ¹ for $\dot{\mathbf{x}}_c$, $\dot{\mathbf{x}}_w$, y_c , and y_w yields the rather unwieldy

$$\dot{\mathbf{x}}_c = [\mathbf{A}_c - k(D_w + R_p + R_s)\mathbf{B}_c\mathbf{C}_c]\mathbf{x}_c + kR_s\mathbf{B}_c\mathbf{C}_w\mathbf{x}_w + k(D_w + R_p)\mathbf{B}_c u, \quad (2.27)$$

$$\dot{\mathbf{x}}_w = kR_s\mathbf{B}_w\mathbf{C}_c\mathbf{x}_c + [\mathbf{A}_w - k(D_c + R_s)\mathbf{B}_w\mathbf{C}_w]\mathbf{x}_w + kD_c\mathbf{B}_w u, \quad (2.28)$$

$$y_c = k(D_w + R_p)R_s\mathbf{C}_c\mathbf{x}_c + kR_s\mathbf{C}_w\mathbf{x}_w + kD_c(D_w + R_p)u, \quad (2.29)$$

$$\text{and } y_w = kD_wR_s\mathbf{C}_c\mathbf{x}_c + k[R_pR_s + D_c(R_p + R_s)]\mathbf{C}_w\mathbf{x}_w + kD_cD_w u, \quad (2.30)$$

$$\text{where } k = \frac{1}{R_s(D_w + R_p) + D_c(D_w + R_p + R_s)}. \quad (2.31)$$

Solving for i_T by substituting Eqs. (2.21), (2.22), (2.29), (2.30) and (2.31) into Eq. (2.20) yields

$$i_T = -k(D_w + R_p)\mathbf{C}_c\mathbf{x}_c - kD_c\mathbf{C}_w\mathbf{x}_w + k(D_c + D_w + R_p)u. \quad (2.32)$$

Consider a state-space system that models the potentiostatic interface to a Randles cell. Such a system would give the current through the cell i_T with respect to the voltage across the cell u . Let \mathbf{x}_R be the associated state-vector for the system, and assume the system consists of matrices

¹The *Non Commutative Algebra Package* for Mathematica verifies these solutions (See Code Listing A.1).

\mathbf{A}_R , \mathbf{B}_R , \mathbf{C}_R and scalar D_R which satisfy

$$\dot{\mathbf{x}}_R = \mathbf{A}_R \mathbf{x}_R + \mathbf{B}_R u \quad (2.33)$$

$$\text{and} \quad i_T = \mathbf{C}_R \mathbf{x}_R + D_R u. \quad (2.34)$$

From Eqs. (2.27), (2.28), and (2.32)

$$\mathbf{x}_R = \begin{bmatrix} \mathbf{x}_c \\ \mathbf{x}_w \end{bmatrix}, \quad (2.35)$$

$$\mathbf{A}_R = \begin{bmatrix} \mathbf{A}_c - \alpha \mathbf{B}_c \mathbf{C}_c & k R_s \mathbf{B}_c \mathbf{C}_w \\ k R_s \mathbf{B}_w \mathbf{C}_c & \mathbf{A}_w - \beta \mathbf{B}_w \mathbf{C}_w \end{bmatrix}, \quad (2.36)$$

$$\mathbf{B}_R = \begin{bmatrix} k(D_w + R_p) \mathbf{B}_c \\ k D_c \mathbf{B}_w \end{bmatrix}, \quad (2.37)$$

$$\mathbf{C}_R = \begin{bmatrix} -k(D_w + R_p) \mathbf{C}_c & -k D_c \mathbf{C}_w \end{bmatrix}, \quad (2.38)$$

$$\text{and} \quad D_R = k(D_c + D_w + R_p), \quad (2.39)$$

where

$$\alpha = k(D_w + R_p + R_s) \quad (2.40)$$

$$\text{and} \quad \beta = k(D_c + R_s). \quad (2.41)$$

2.4. Accuracy of the State-Space Model

It is desirable to compare the accuracy of the state-space model to the corresponding theoretical Randles circuit. Considering that cell impedance (for ω between 0.1Hz to 1MHz) is the desired outcome of electrochemical data collection, it is fitting to compare the impedance of the model to its theoretical values.

Given the state-space representation for a Randles circuit from Eqs. (2.36), (2.37), (2.38) and (2.39), the Laplace transform of the state-transition matrix [18, Eq. 3.49] is given as

$$\Phi(s) = (s\mathbf{I} - \mathbf{A}_R)^{-1}. \quad (2.42)$$

Using the above definition, the continuous transfer function for the system [18, Eq. 3.62] is

$$H(s) = \mathbf{C}_R \Phi(s) \mathbf{B}_R + D_R. \quad (2.43)$$

Recall that this system gives the current through a Randles cell $i_T(t)$ as a function of voltage $u(t)$. Consider the following relationship in the frequency domain:

$$\mathcal{L}\{i_T(t)\}(s) = H(s) \mathcal{L}\{u(t)\}(s). \quad (2.44)$$

Solving for $H(s)$ gives

$$H(s) = \frac{\mathcal{L}\{u(t)\}(s)}{\mathcal{L}\{i_T(t)\}(s)}. \quad (2.45)$$

This results in a reciprocal relationship between the model's transfer function $H(s)$ for $s = j\omega$ and its impedance $Z_m(\omega)$:

$$Z_m(\omega) = \frac{1}{H(j\omega)}. \quad (2.46)$$

The theoretical impedance $Z_{th}(\omega)$ for a given Randles cell can be determined by combining the impedances of the components across the cell. This is found to be

$$Z_{th}(\omega) = R_s + \frac{1}{C_{dl}j\omega + \frac{1}{R_p + Z_W(\omega)}}, \quad (2.47)$$

where $Z_W(\omega)$ is the theoretical impedance of a Warburg element from Eq. (1.11) with Warburg coefficient σ .

2.4.1. Quantifying Error

Let the error between the theoretical impedance from Eq. (2.47) and the model impedance from Eq. (2.46) be defined as

$$\text{Err}(\omega) = \frac{|Z_{\text{th}}(\omega) - Z_{\text{m}}(\omega)|}{|Z_{\text{th}}(\omega)|}. \quad (2.48)$$

This definition of error serves to normalize the magnitude of the difference between the theoretical impedance and the model impedance with respect to the theoretical impedance.

Table 2.1. Test cases for different parameter values

Model #	R_s	R_p	C_{dl}	σ	Δ_ϕ
Model 1	20 Ω	250 Ω	40 μF	0.01	$8 \cdot 10^{-4}$
Model 2	20 Ω	250 Ω	40 μF	10	$8 \cdot 10^{-4}$
Model 3	10 Ω	300 Ω	40 μF	50	$8 \cdot 10^{-4}$
Model 4	10 Ω	1K Ω	40 μF	150	$8 \cdot 10^{-4}$

A set of four test-cases to explore the accuracy of the state-space representation are given in Table 2.1. The parameters of each model were selected based off example scenarios given by Gamry Instruments [5]. For each model, the polarization resistivity R_p and Warburg coefficient σ increase while solution resistivity R_s decreases and the double layer capacitance C_{dl} and maximum allowable ripple Δ_ϕ remain fixed. Plots of the normalized error for each model (with a log-log scale) are given in Figs. 2.2, 2.3, 2.4, and 2.5.

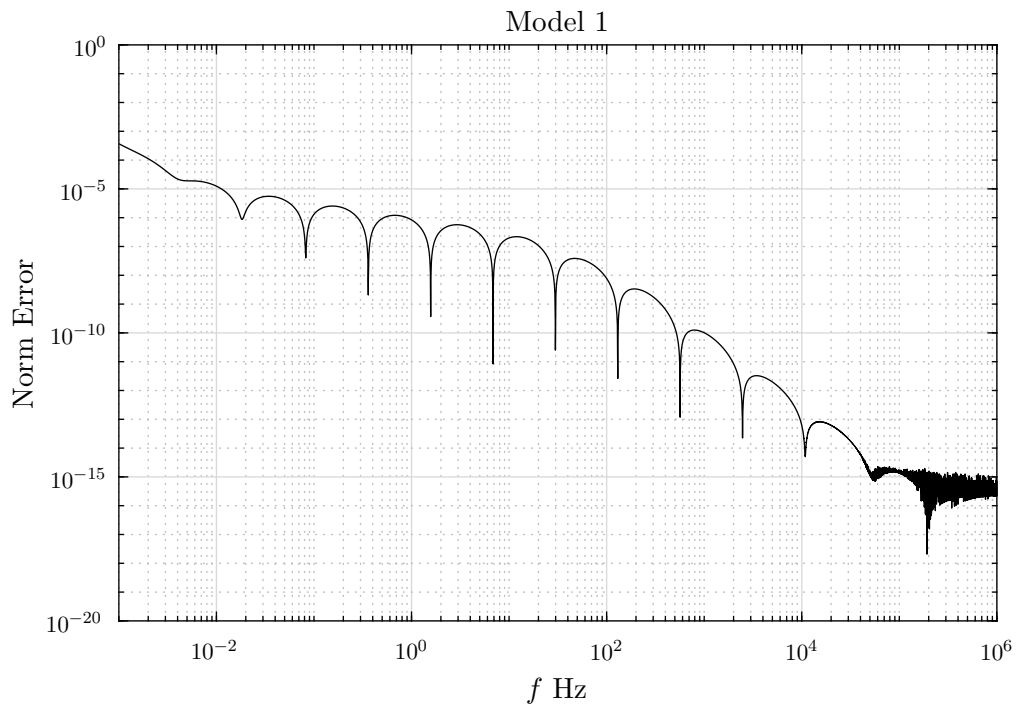


Figure 2.2. Normalized error for model 1 (system order $m = 17$).

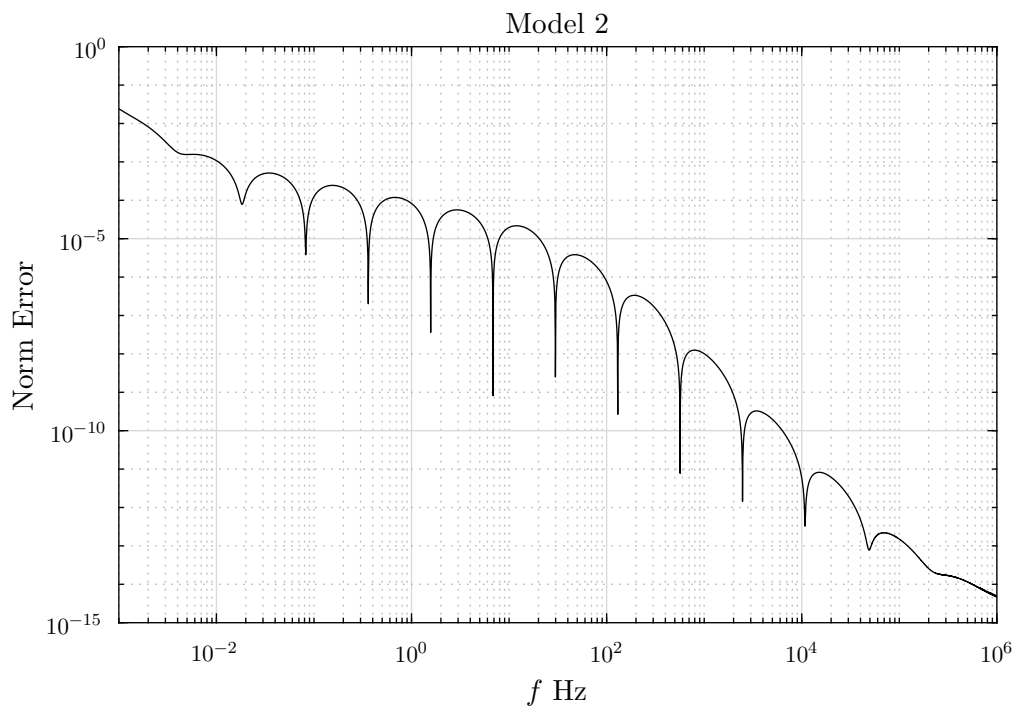


Figure 2.3. Normalized error for model 2 (system order $m = 17$).

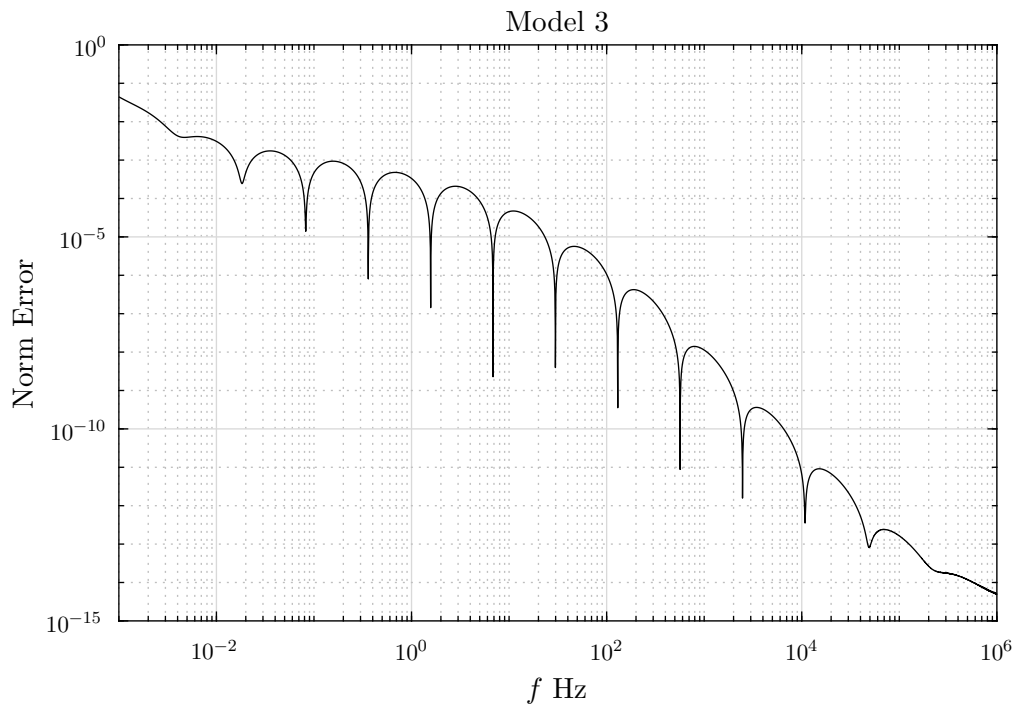


Figure 2.4. Normalized error for model 3 (system order $m = 17$).

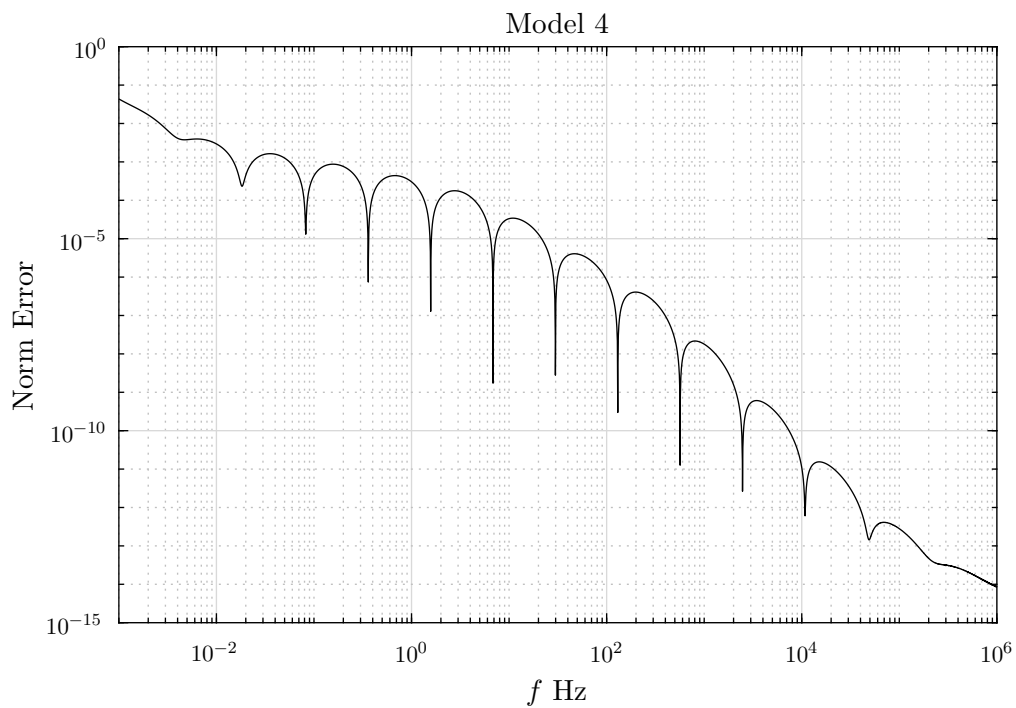


Figure 2.5. Normalized error for model 4 (system order $m = 17$).

As demonstrated by these figures, the normalized error of the model is quite small for each model (less than 10^{-1}). Note the noise-like disturbance present in the upper frequencies of Fig. 2.2. Given the extremely low magnitude of the error (less than 10^{-15}), the double floating-point representation employed in the simulation begins to manifest noticeable deviations from the expected results due to round-off errors [19]. Note that the shape of the normalized error remains consistent (despite the aforementioned distortion in Fig. 2.2); it merely shifts upward (becomes greater) for each consecutive model.

The consistency in shape is due to the consistency of the Δ_ϕ parameter which controls the maximum allowable phase ripple for the CPE approximation. The upward shift is due to the σ parameter, which controls the prominence of the Warburg element. Since the Warburg element is the only component modeled by an approximation, it is therefore the source of the deviation from the theoretical impedance (i.e. the error). Thus, it follows that increasing the strength of this component also increases the magnitude of the error.

2.4.2. Nyquist Plots

As mentioned in Sec. 1.4, Nyquist plots can offer insight into equivalent circuit component parameters (e.g. R_s , R_p , C_{dl} and σ for a Randles cell). To aid in analysis, Nyquist plots of the state-space representation for each model in Table 2.1 are depicted in Figs. 2.6, 2.7, 2.8, and 2.9. Given the small magnitude of the normalized error, the Nyquist plot of each model is indistinguishable from the corresponding theoretical plot. Note the tail-like protrusions off the arc-like features in these figures. This is indicative of a strong Warburg impedance [5], [1, p. 268]. It is therefore understandable that this tail becomes more prominent as the strength of the Warburg element is increased.

Having established the accuracy of the continuous-time state-space representation, the process of digital hardware implementation can now be considered. Given that synchronous digital systems are clocked and execute instructions at consistent intervals, a discretization of the continuous-time representation is needed.

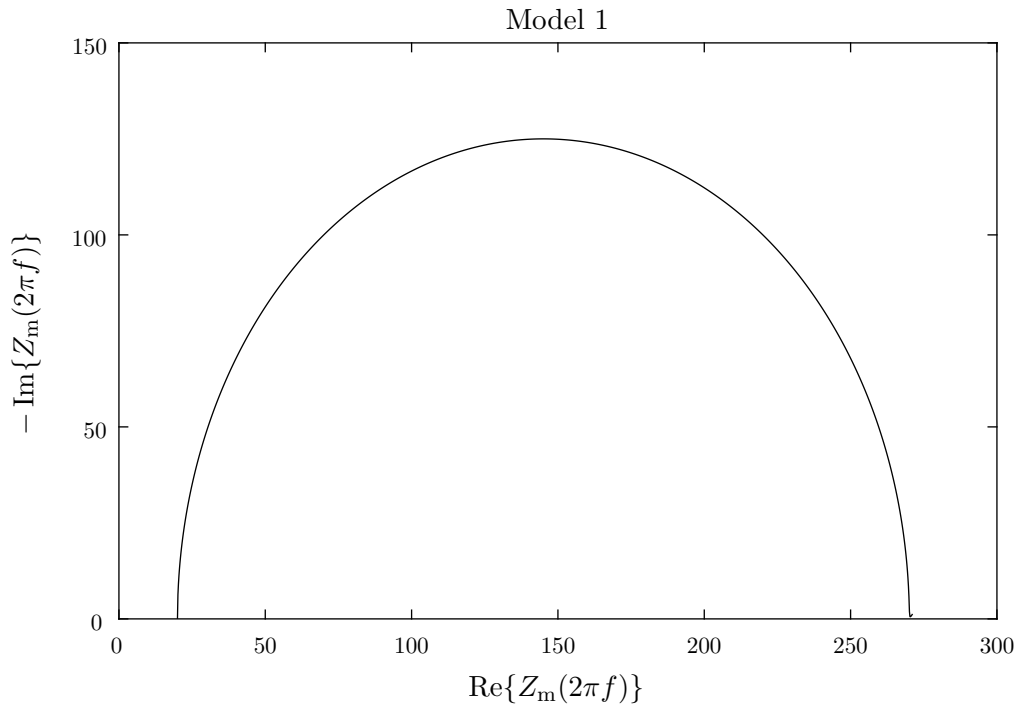


Figure 2.6. Nyquist plot for model 1 (system order $m = 17$).

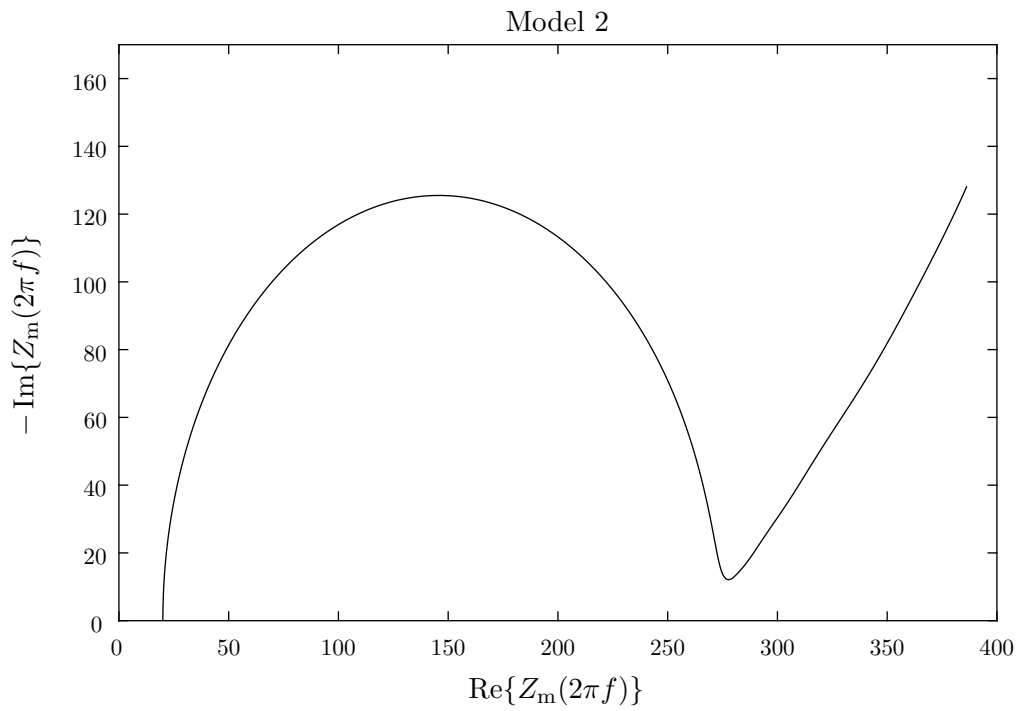


Figure 2.7. Nyquist plot for model 2 (system order $m = 17$).

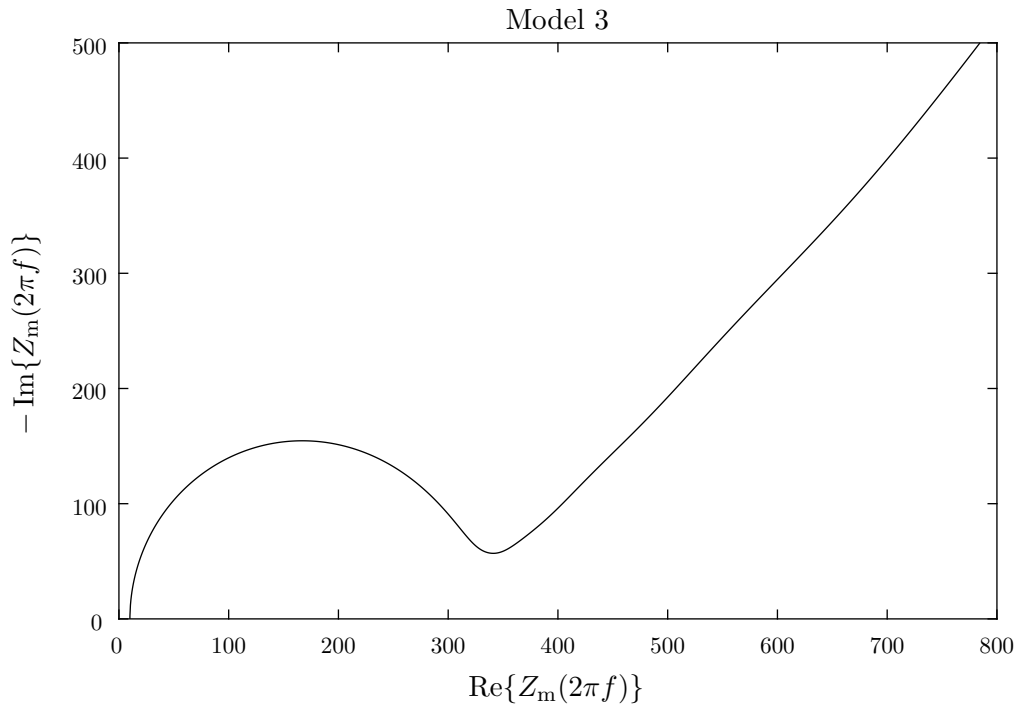


Figure 2.8. Nyquist plot for model 3 (system order $m = 17$).

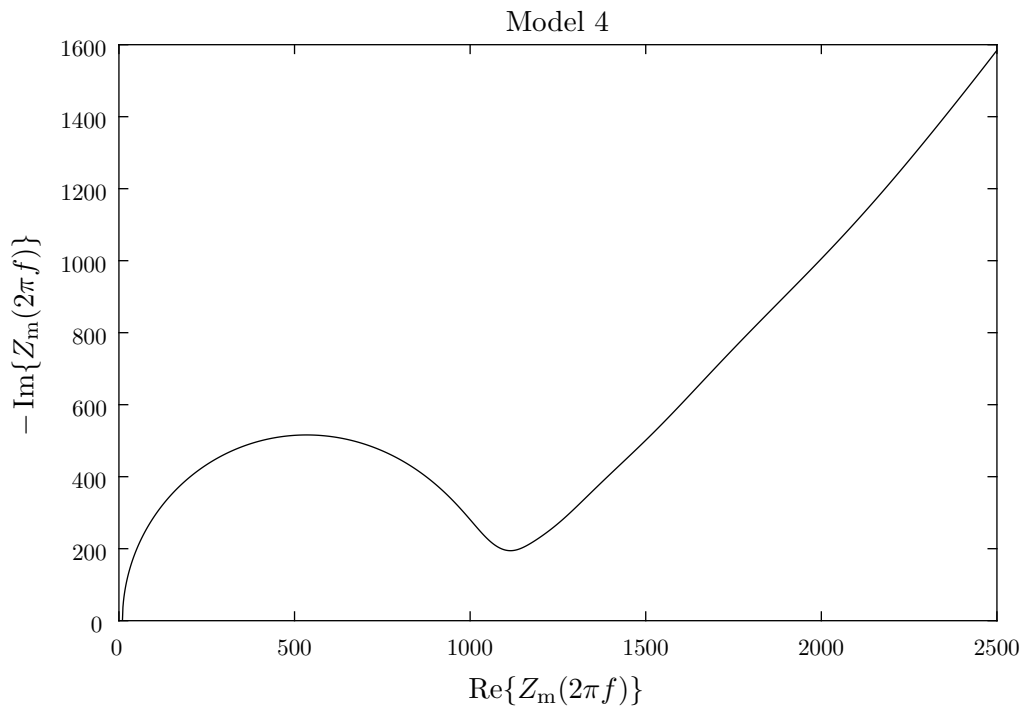


Figure 2.9. Nyquist plot for model 4 (system order $m = 17$).

3. METHODS OF DIGITAL IMPLEMENTATION

In order to translate the state-space model of a general Randle cell's impedance response given by Eqs. (2.36), (2.37), (2.38), (2.39) and (2.40) into a physical system to calibrate EIS hardware, it is necessary to translate the output of the state-space impedance response to a current driving circuit. In this translation, the output of the impedance response would be proportional to the current driven between the WE and the CE of the target instrument. Such a realization is best suited for a microprocessor that implements a digital filter due to its ability to be reprogrammed to model different parameter configurations (R_s , R_p , C_{dl} , σ and Δ_ϕ). Since the output of the microprocessor will be a voltage potential driving a current source, it may be necessary to scale the impedance response by a predetermined amount and introducing an additional DC offset before sending it to the *digital-to-analog converter* (DAC) of the microprocessor. This additional gain factor and DC offset would be determined by the requirements of the current driver and the output range of the DAC. The general input/output requirements for a standard microprocessor with a DAC are given in Table. 3.1.

Table 3.1. Generalized input/output mapping for realization on a microprocessor with a DAC.

Property	Units	Interpretation
Signal Input	V	Input potential from instrument
Signal Output	V	<i>Proportional to and offset from</i> the current driven to the instrument

Given that the state-space relations derived in Eqs. (2.36), (2.37), (2.38), (2.39) and (2.40) model a continuous time system, implementation on digital hardware requires the system to be discretized (e.g. conversion from the s -domain to the z -domain). For this process and the particular method of discretization chosen (the *matched z -transform method*, see 3.2.1) it is necessary to extract the poles, zeros, and overall gain of the state-space system.

3.1. Calculating Poles and Zeros from State-Space

The process of finding poles, zeros and overall gain from a generalized state-space representation involves the calculation of eigenvalues to determine the poles, the zeros are found as the

solution to a generalized eigenvalue problem, and the gain is calculated as the first nonzero Markov parameter [20]. The algorithms which compute these values are beyond the scope of this thesis, rather such algorithms/calculations are handled within MATLAB (See Code Listing A.3). The pole/zero plots for the models in Table 2.1 are given in Figs. 3.1, 3.2, 3.3, and 3.4. Note that for each model both the poles and zeros lie on the real axis.

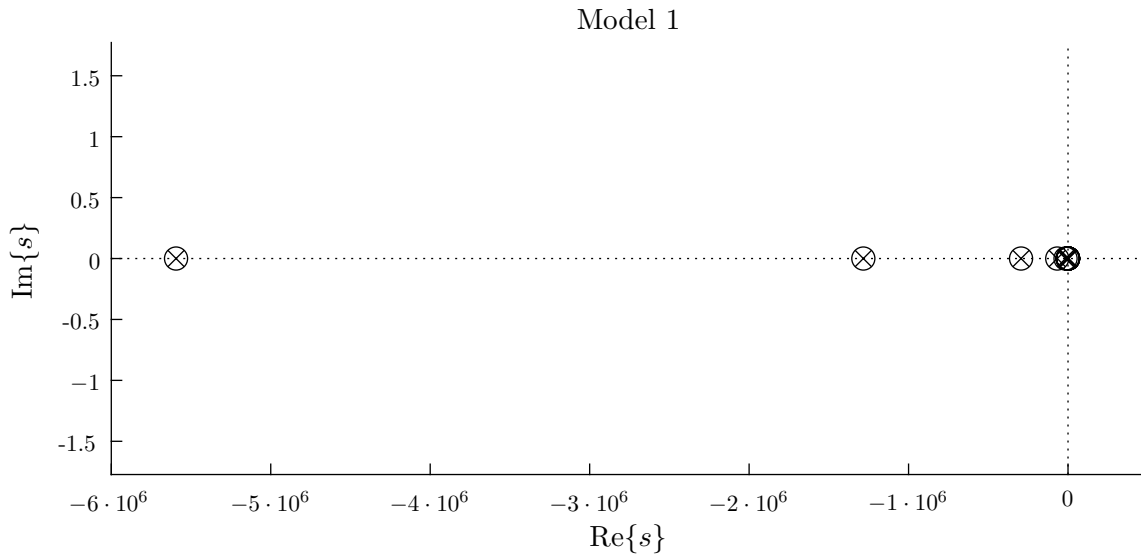


Figure 3.1. Pole/zero plot in the s -domain for model 1 (system order $m = 17$).

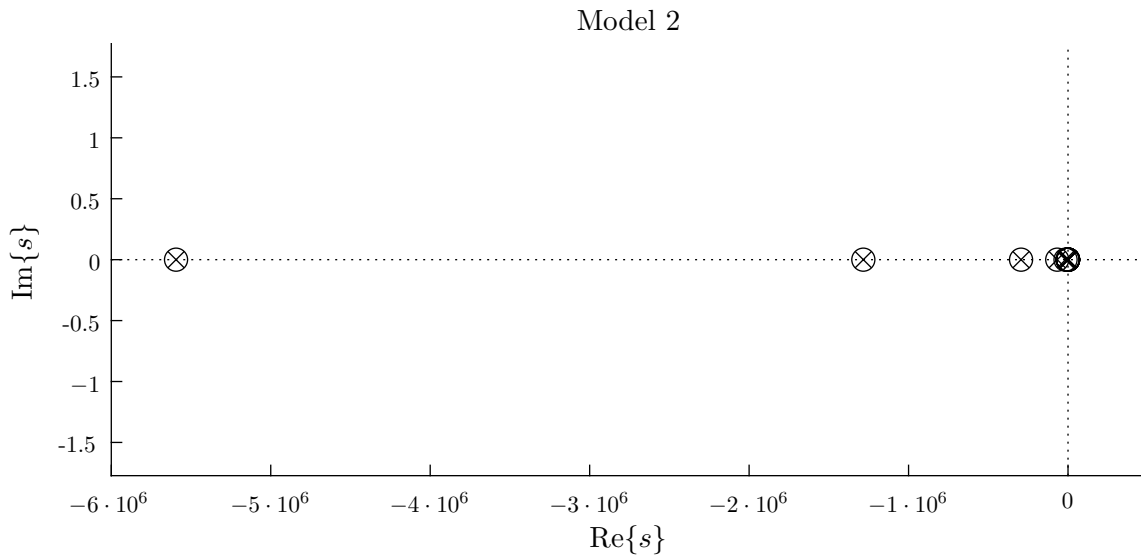


Figure 3.2. Pole/zero plot in the s -domain for model 2 (system order $m = 17$).

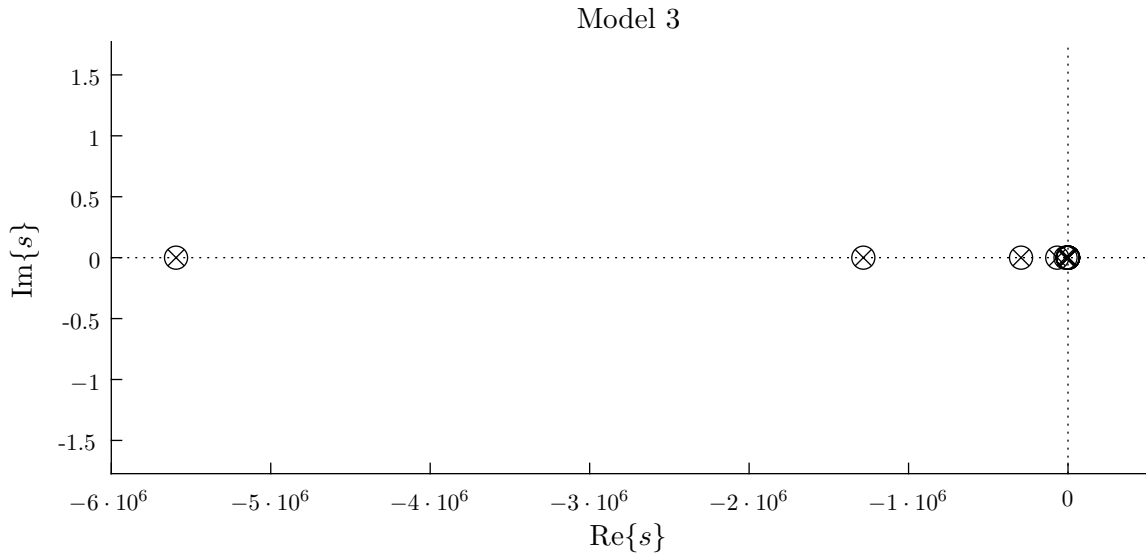


Figure 3.3. Pole/zero plot in the s -domain for model 3 (system order $m = 17$).

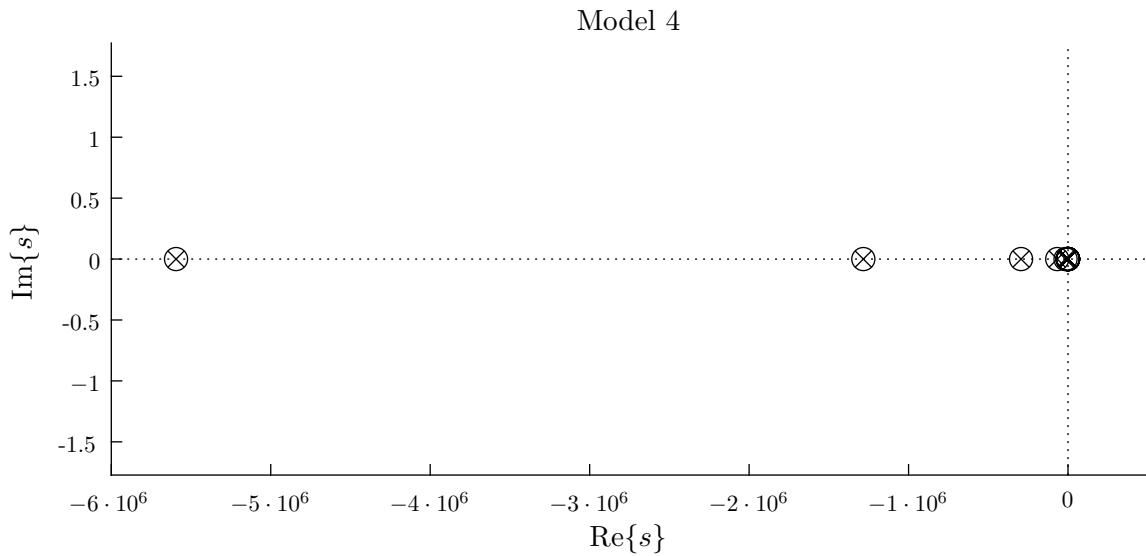


Figure 3.4. Pole/zero plot in the s -domain for model 4 (system order $m = 17$).

3.2. System Discretization

Given that microprocessors are clocked and execute various operations on a set of fixed intervals, it is necessary to discretize continuous systems using a particular sampling rate. This sampling frequency regulates the ability of the system to respond a certain way beyond a certain frequency (this process is called *aliasing* and the frequency after which this occurs is often called

the *Nyquist frequency*). Therefore, in order to achieve the correct response up to a given frequency f_0 (in Hz), the target must be capable of delivering an output at the corresponding sampling rate F_s (in Hz). This relationship between f_0 and F_s is given by the Shannon-Nyquist theorem

$$F_s \geq 2f_0. \quad (3.1)$$

Given that most experiments in EIS do not include responses beyond 1MHz [5], this can be considered a reasonable f_0 select. The Shannon-Nyquist theorem from Eq. (3.1) gives that the required sampling-rate should be at least 2MHz. In order to introduce some headroom to work with, the sampling rate $F_s = 2.2\text{MHz}$ is used in all future calculations and test cases.

There are several standard methods for discretizing continuous systems. The *impulse invariance* method, the *limit definition of derivatives*, the *bilinear transform*, and the *matched z -transform* method [?]. Unlike the bilinear transform which struggles to represent a system's response at high frequencies [21], and the impulse invariance method that suffers from window distortion and frequency aliasing, the matched z -transform maps the poles and zeros of the system simply. This property of directly mapping poles/zeros using a consistent rule makes the matched z -transform a particularly attractive option considering the poles/zeros of the models are known.

3.2.1. Matched Z-Transform Method

The matched z -transform maps each singularity to the z -plane with the following mapping

$$z = e^{sT} \quad (3.2)$$

where T is the sampling interval $1/F_s$. The poles and zeros from Sec. 3.2 are mapped following Eq. (3.2). A gain correction factor is then determined by dividing the gain of the continuous $H(s)$ at $s = 0$ by the gain of the discrete system $H(z)$ at $z = 1$ (see the Code Listing A.4). This discretized system now has the poles p_{z_i} , zeros z_{z_i} and overall gain k_z .

A pole/zero plot for the first model is given in Fig. 3.5. Note that all of the system's poles and zeros lie on the real axis and most are clustered closely around unity. The presence of poles and zeros on the real axis is to be expected from Eq. (3.2) as each pole/zero is a real number that is mapped to an exponential raised to a real number, thus remaining a real number. Each model

in Table 2.1 will produce a similar pattern of poles and zeros. Such a view is not beneficial for the purposes of analysis. Therefore, views magnified around the real axis of the analogous z -domain pole/zero plots for each model in Table 2.1 are given in Figs. 3.6, 3.7, 3.8, and 3.9.

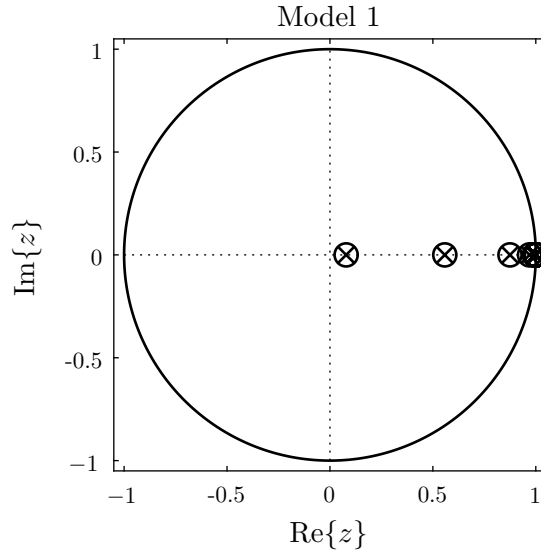


Figure 3.5. Pole/zero plot in the z -domain for model 1 (system order $m = 17$).

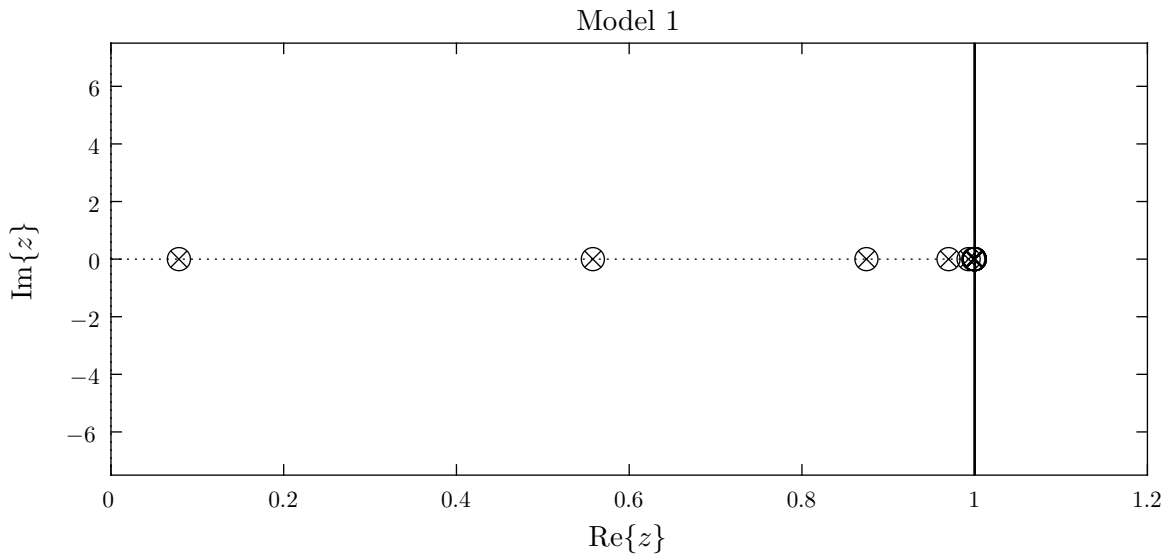


Figure 3.6. Magnified pole/zero plot in the z -domain for model 1 (system order $m = 17$).

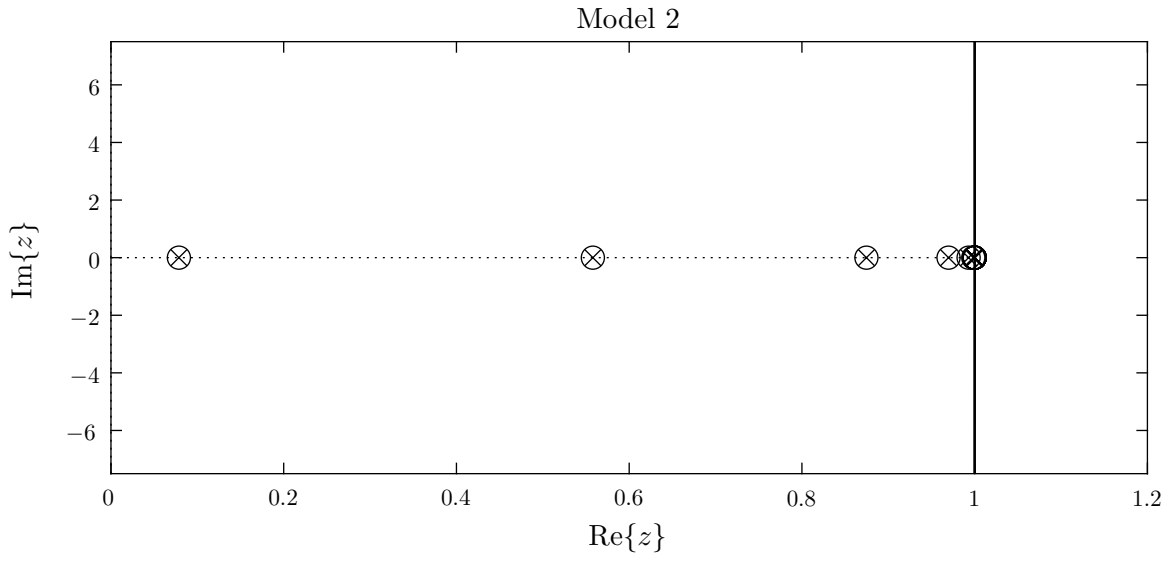


Figure 3.7. Magnified pole/zero plot in the z -domain for model 2 (system order $m = 17$).

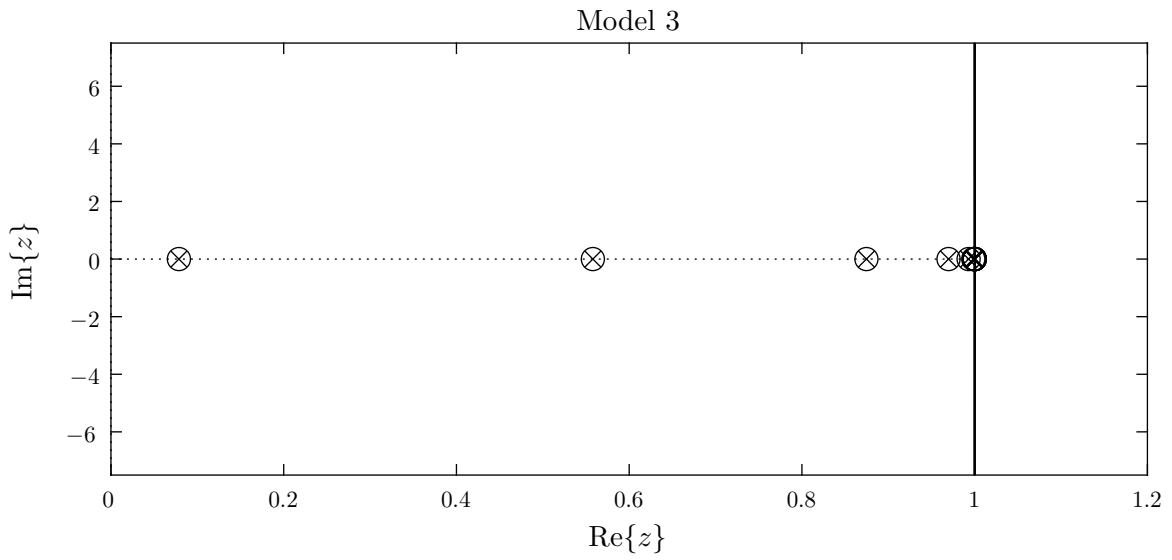


Figure 3.8. Magnified pole/zero plot in the z -domain for model 3 (system order $m = 17$).

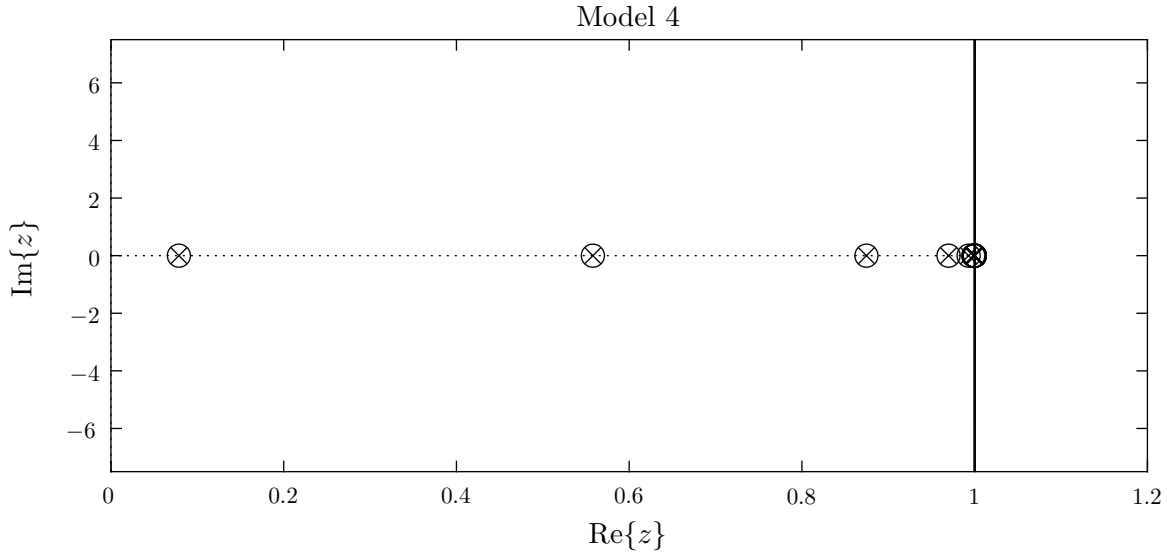


Figure 3.9. Magnified pole/zero plot in the z -domain for model 4 (system order $m = 17$).

3.3. Internal Filter Structure

Digital filters can be divided into two distinct classes: those that incorporate feedback, called infinite impulse response (IIR) filters, and those that do not, called finite impulse response (FIR) filters. Given the presence of poles outside the origin of the z -domain, indicative of feedback, for the models given in Table 2.1, these systems best lend themselves to an IIR realization¹.

Higher-order filters are usually realized as a combination of subfilters [22, p. 508]. These subfilters are typically second order (being the smallest order capable of realizing pairs of complex conjugate roots). Such subfilters can be configured in canonical direct forms, in canonical transposed forms, or in more exotic manners. This collection of subfilters is then fed together (in either series or parallel) to produce a final output.

A cascade configuration is typically considered a good general-purpose strategy [22, p. 508] for combining subfilters. A typical aim in determining subfilter coefficients is the minimization of potential instabilities caused by floating/fixed-point inaccuracies or other sources of imperfection. As such, a potential goal for each subfilter is the minimization of peak amplitudes in the frequency response. A straightforward method [22, p. 508] for achieving this end is to pair poles with the closest zeros.

¹Poles stacked on the origin and only the origin appear in the transfer function for FIR filters

Unfortunately, the standard second order subfilter configurations (direct, transposed etc.) have difficulty encoding poles and zeros which lay close to the real axis in the z -domain [407]. Unfortunately, for each given model in Table 2.1, both the poles and zeros lie exclusively along the real axis (Sec. 3.2). Some alternative second order setups that attempt to mitigate the poor representation near the real axis assume that poles and zeros come in complex conjugate pairs. The configuration of subfilters chosen to realize the overall filters for the models given in Table 2.1, consist of a cascade of first order (single-pole/single-zero filters). Such a configuration was chosen as the most straightforward and simplest way to avoid the inaccuracies caused by finite word lengths. In selecting these first order subfilter coefficients, each pole was still paired with the closest zero for the sake of minimizing potential instabilities (see Code Listing A.5).

3.4. Effects of Finite Word-Length on Accuracy

Some lower-end processors lack a dedicated floating-point Arithmetic Logic Unit (ALU). For such processors, fractional numbers can be implemented using a fixed-point representation. This is differentiated from floating point representations in its lack of an exponential scaling term, instead consisting of only a mantissa. Given that the poles and zeros fall within the unit circle for each model from Sec. 2.4.1, each subfilter coefficient (including the final gain terms) lie between $(0, 1)$. This allows for all the bits in word-length to be used for encoding the fractional portion of the coefficient. In this case, fixed pointed representations will be more precise than floating point representations.

To assess the effect bit resolution has on the accuracy of the discretized state-space representation, test cases were created in which the subfilter coefficients were restricted to fixed-point representations with varying bit resolutions in accordance with the manner previously described. If any bit resolutions produced subfilters in which the pole and zero were the same number, that subfilter was removed (subfilters with such properties cancel themselves out and can only cause problems in implementation). The component values (held constant) along with the fixed-point bit resolution for each test case are given in Table 3.2.

The pole/zero plots, zoomed-in along the positive real axis, of each implementation are given in Figs. 3.10, 3.12, and 3.14. In addition, plots of the magnitude and phase response of the fixed-point approximation for each implementation in comparison to the theoretical is given

Table 3.2. Test cases for different word lengths.

Implementation #	R_s	R_p	C_{dl}	σ	Δ_ϕ	Bit Res.
Implementation 1	20Ω	250Ω	$40\mu\text{F}$	10	$8 \cdot 10^{-4}$	16
Implementation 2	20Ω	250Ω	$40\mu\text{F}$	10	$8 \cdot 10^{-4}$	32
Implementation 3	20Ω	250Ω	$40\mu\text{F}$	10	$8 \cdot 10^{-4}$	64

in Figs. 3.11, 3.13, and 3.15. These plots illustrate the frequency bands in which the fixed-point approximation diverges from the theoretical response.

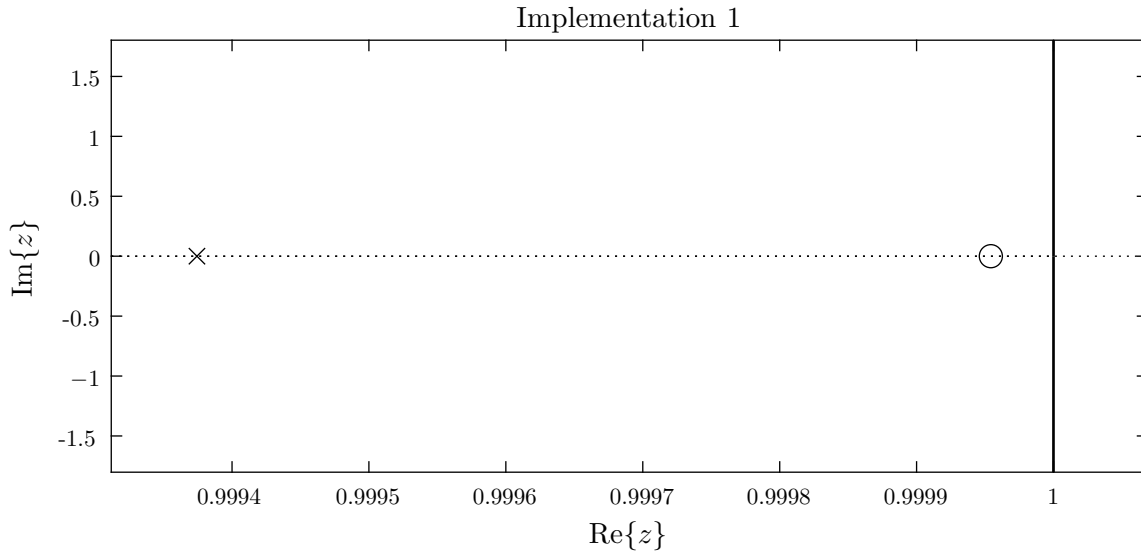


Figure 3.10. Magnified pole/zero plot of implementation 1 (system order $m = 1$).

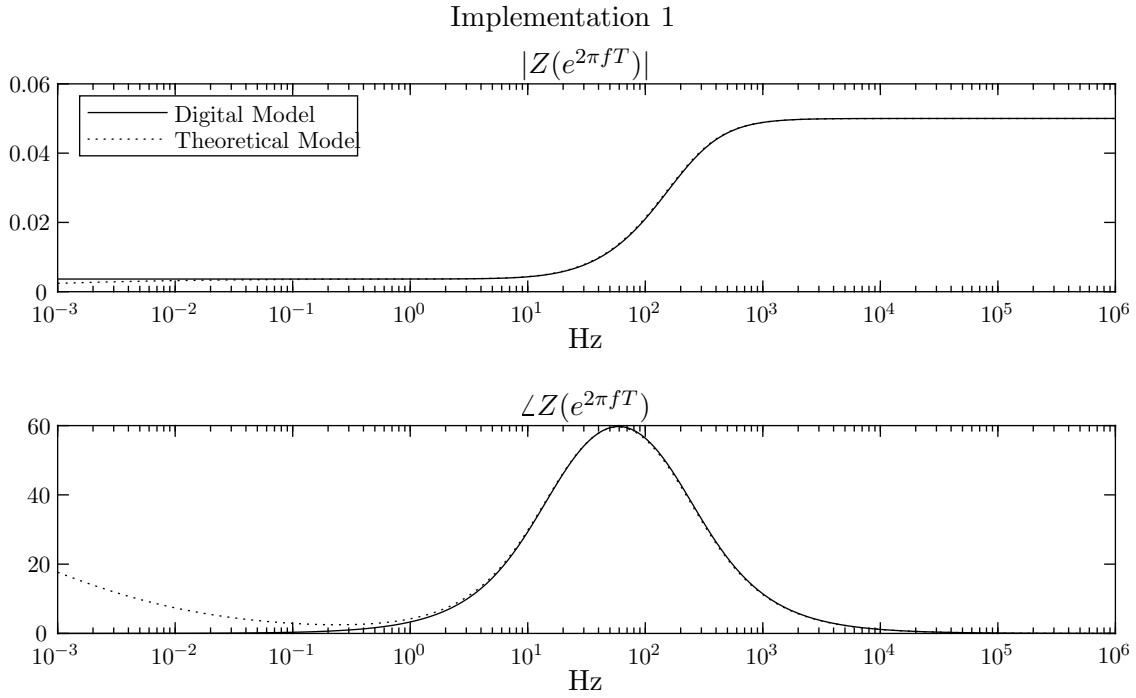


Figure 3.11. Frequency response of implementation 1 (system order $m = 1$) compared to the theoretical response.

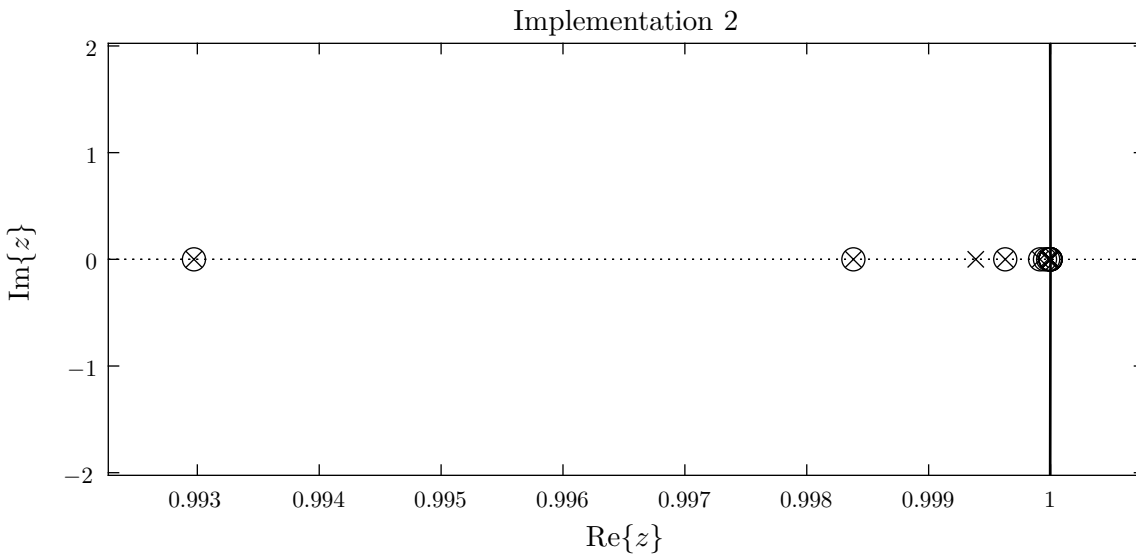


Figure 3.12. Magnified pole/zero plot of implementation 2 (system order $m = 13$).

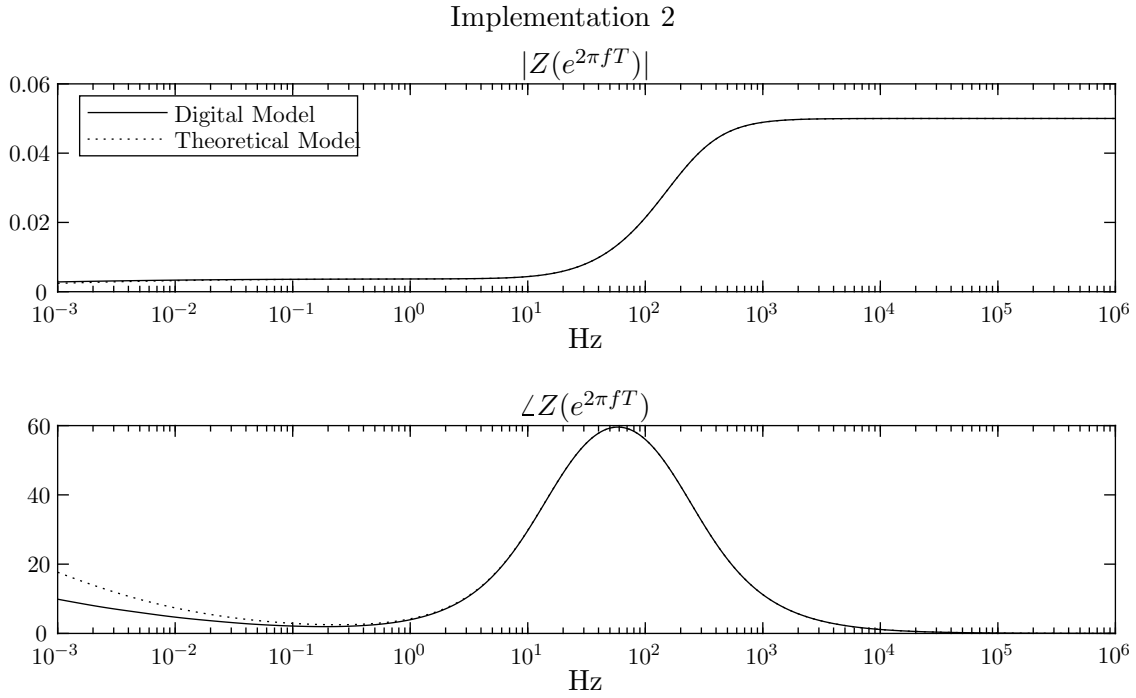


Figure 3.13. Frequency response of implementation 2 (system order $m = 13$) compared to the theoretical response.

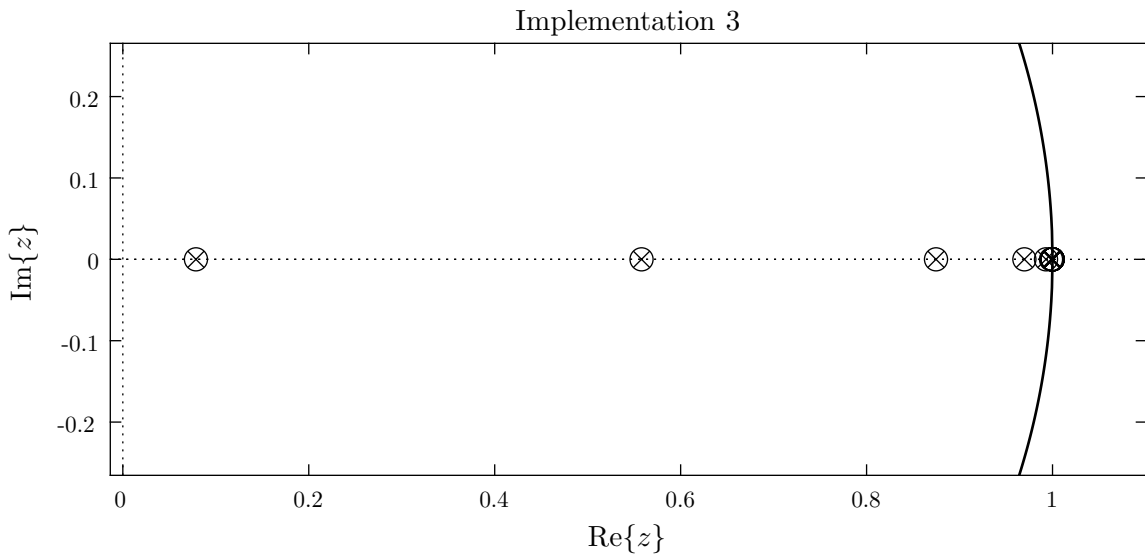


Figure 3.14. Magnified pole/zero plot of implementation 3 (system order $m = 17$).

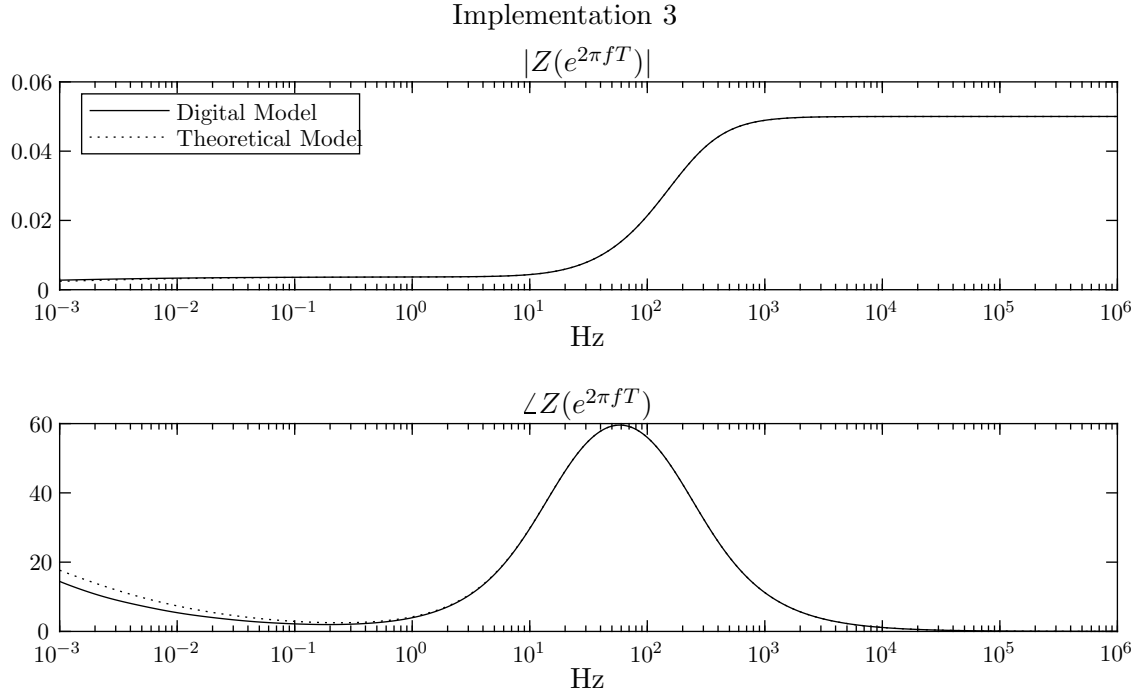


Figure 3.15. Frequency response of implementation 3 (system order $m = 17$) compared to the theoretical response.

It can be seen in Fig. 3.11, that the phase response deviates substantially from the intended behavior below 1 Hz. The phase response of the implementations approach that of the theoretical (the implementations become more accurate) from Fig. 3.13 to Fig. 3.15 for each consecutive implementation.

From the calculations in Sec. 1.4 it was shown that as frequencies decrease, the more linear behavior caused by the Warburg element dominates the impedance response. From Sec. 2, all but one of the system's poles/zeros are introduced by the Warburg Element approximation (the remaining pole/zero pair is introduced by the capacitor C_{dl}). Since few non-matching pole/zero pairs exist in Fig. 3.10 it can be inferred that the Warburg element approximation will not be accurately represented. This is confirmed in Fig. 3.11. It can be surmised that as the number of non-matching pole/zero pairs increase, the accuracy of the Warburg element approximation (whose effect is most prominent in lower frequencies) will improve. This is borne out in Figs. 3.13 and 3.15 and the number of pole/zero pairs increase from Fig. 3.12 to Fig. 3.14.

4. FUTURE DIRECTION AND CONCLUSION

4.1. Future Direction

The *next steps* in implementation would include the selection of a particular current-driving circuit and microprocessor considering the restraints mentioned in Sec. 3. Such a processor would also require a DAC compatible and capable of driving the selected current source. The microprocessor should be able to implement the subfilter strategy outlined in Sec. 3.3 within the appropriate sampling interval $1/22\text{k} \approx 45.5\mu\text{s}$ (see Sec. 3.2).

Even if these restraints are followed, there will potentially be unexpected behavior caused by the response of the target instrumentation. Modern instrumentation attempts to alleviate this problem when properly configured [15]. In particular, *i_R compensation* may interfere with the expected behavior of the model.

4.1.1. Consideration of Equipment Response

Certain equipment may compensate for expected discrepancies that do not originate within the electrochemical cell. For example, transmission line effects that occur in the cables connecting the electrodes to the potentiostat (typical shielded cables introduce a capacitance of approximately 50 pF per cm [11]). Equipment that expects and compensates for certain deviations from ideal behavior may not be properly calibrated by this system. It is not uncommon for modern instrumentation such as Gamry Instruments' Reference 600+ to feature such compensation measures [15].

For most electrochemical experiments, the Faradaic impedance at the interface of the working electrode (represented as the portion of a Randles cell in Fig. 1.5 that excludes the initial resistor R_s) is of greatest interest [1, p. 30]. Rather than compensating for the voltage drop caused by R_s (commonly called *i_R*) during post processing, some experiments may attempt to remove the effect of *iR* in the experimental setup. Proper placement of the RE and the use of a Luggin capillary can assist in minimizing this *i_R* [1, p. 33].

For experiments with small solution resistivities, this voltage drop is insignificant. Another common method of compensating for *i_R* during the experiment introduces an *i_R* compensator circuit. Such devices add complexity into the calibration process, given that there is not purposeful

resistance introduced between the WE and the CE. The addition of compensators that expect such a resistivity may cause the target equipment to be improperly calibrated.

Additional deviations from the ideal electrochemical cell are often introduced by the reference electrode (RE). Depending on the RE's material and the composition of the surrounding electrolytic solution, the RE itself may manifest its own resistance and capacitance. Thus, the RE begins to function as a lowpass filter. Fortunately, the cutoff frequency for common RE setups is usually around 1.5MhZ [1] which is well within the range of most AC impedance experiments. The RC filter can still distort the cell's response via its introduction of phase delay. Instruments that compensate for the frequency response of a particular RE setup will not be properly calibrated using this procedure.

4.1.2. Multi-Rate Implementation

Given the phenomena observed in Figs. 3.6, 3.7, 3.8, and 3.9 in which poles and zeros are clustered close to DC, a potential future action would be to introduce a multi-rate system. For systems with lower sample-rates, the poles/zeros near DC will be pulled toward the origin and will require less precision to encode. Lower-rate systems could be employed for input frequencies below a given threshold while higher-rate systems would be employed above said threshold. This would have the potential effect of increasing the accuracy of the phase response for lower frequencies (deviation from the theoretical is still noticeable in Fig. 3.15). Such an implementation is ripe for future exploration.

4.2. Conclusion

In summary, this thesis gave a general background on the theory and applications of EIS which provided a motivation for creating a digital model of an electrochemical cell for the purposes of confirming and calibrating EIS instrumentation (Sec. 1.1.1). The Randles equivalent circuit was introduced as an existing model that captures the behavior of a large variety of electrochemical reactions in EIS. An overview of the theoretical Warburg element as a sub-type of the class of components known as constant phase elements was detailed and an explanation of its behavior in terms of impedance was presented (Sec. 1.3). A method described by Valsa et al. [2] to approximate CPEs over a range of frequencies was provided (Sec. 1.6). This method was then used to construct a series of state-space relations with the eventual goal of extracting the poles, zeros and overall gain from this representation 2) A brief explanation on the algorithm of extracting poles/zeros/gain

provided by MATLAB is detailed (Sec. 3.1), followed by a discussion on discretization and sampling (Sec. 3.2). The matched z -transform was then introduced as the means to discretize the poles/zeros/gain to facilitate digital realization (Sec. 3.2.1). An analysis of realization methods, along with concerns regarding the difficulty in implementing a filter capable of accurately recreating the responses for a previous set of test cases were given (Sec. 3.3). From this, a realization approach was selected. Finally, an exploration of the effects caused by fixed-point approximations is presented (Sec. 3.4).

This thesis provides a novel representation of a Randles cell approximation and derives requirements and suggestions for realizing digital implementations of the systems described in these relations. It provides a brief analysis of the effects imposed by practical restrictions. The information presented in this thesis is a suitable starting point and reference for the creation of high accuracy digital models.

REFERENCES

- [1] D. D. Macdonald, *Transient Techniques in Electrochemistry*. Plenum Press, 1977.
- [2] J. Valsa, P. Dvořák, and M. Friedl, “Network model of the cpe,” *Radio Engineering*, vol. 20, no. 3, pp. 619–626, 2011.
- [3] R. G. Kelly, *Electrochemical techniques in corrosion science and engineering*. Dekker, 2003.
- [4] K. Jiří, D. Jiří, and L. Kavan, *Principles of electrochemistry*, 2nd ed. Wiley, 1993.
- [5] Gamry Instruments, “Basics of electrochemical impedance spectroscopy.” [Online]. Available: <https://www.gamry.com/application-notes/EIS/basics-of-electrochemical-impedance-spectroscopy/>
- [6] A. Sandschulte, R. Ferrero, L. Hardwick, and E. Patelli, “Approach to wide-frequency battery impedance measurements in commercial applications,” in *2019 IEEE 10th International Workshop on Applied Measurements for Power Systems (AMPS)*, Sep. 2019, pp. 1–6.
- [7] S. Uno, “Modeling and simulation of electrochemical biosensors based on cmos lsi chips,” in *2019 Electron Devices Technology and Manufacturing Conference (EDTM)*, 2019, pp. 240–242.
- [8] D. R. Crow, *Principles and Applications of Electrochemistry*, 2nd ed. Chapman and Hall Ltd, 1979.
- [9] Gamry Instruments, “Getting started with electrochemical corrosion measurement.” [Online]. Available: <https://www.gamry.com/application-notes/corrosion-coatings/basics-of-electrochemical-corrosion-measurements/>
- [10] —, “Potentiostat fundamentals.” [Online]. Available: <https://www.gamry.com/application-notes/instrumentation/potentiostat-fundamentals/>
- [11] —, “Reference electrodes.” [Online]. Available: <https://www.gamry.com/application-notes/instrumentation/reference-electrodes/>

- [12] D. E. Smith, in *Electroanalytical Chemistry*, A. J. Bard, Ed. New York: Marcel Dekker, 1966, vol. 1, pp. 1–155.
- [13] T. Berzins and P. Delahay, “Eine methode für das studium schneller elektrodenreaktionen,” *zeitschrift für elektrochemie*, p. 792, 1955.
- [14] Greef and Robert, “Instruments for use in electrode process research,” *Journal of Physics E: Scientific Instruments*, vol. 11, no. 1, pp. 1–12, 1978.
- [15] Gamry Instruments, “Reference 600+ potentiostat/galvanostat/zra operator’s manual,” 2019. [Online]. Available: <https://www.gamry.com/assets/Uploads/Reference-600+-V1-rev-6-3.pdf>
- [16] C. S. Cheng, H. S. H. Chung, and R. W. H. Lau, “Time-domain modeling of constant phase element for simulation of lithium batteries under arbitrary charging and discharging current profiles.” IEEE, 2017.
- [17] A. Fonseca and R. Green, “State-space randles cell model for instrument calibration,” in *The Annual IEEE Canadian Conference on Electrical and Computer Engineering*, 2020.
- [18] B. Friedland, *Control System Design: An Introduction to State-Space Methods*. Dover Publications, Inc., 2005.
- [19] MathWorks, “Matlab online documentation.” [Online]. Available: https://www.mathworks.com/help/matlab/matlab_prog/floating-point-numbers.html
- [20] —, “Matlab online documentation.” [Online]. Available: <https://www.mathworks.com/help/signal/ref/ss2zp.html>
- [21] C. Ojas and G. David, “Optimizing the magnitude response of matched z-transform filters (“mzti”) for loudspeaker equalization,” in *32nd International Conference: DSP For Loudspeakers*, 2007.
- [22] B. P. Lathi and R. A. Green, *Essentials of Digital Signal Processing*. Cambridge University Press, 2014.

- [23] Gamry Instruments, "Understanding ir compensation." [Online]. Available: <https://www.gamry.com/application-notes/instrumentation/understanding-ir-compensation/>
- [24] R. Buchanan and E. Stansbury, "4 - electrochemical corrosion," in *Handbook of Environmental Degradation of Materials*, 2nd ed., M. Kutz, Ed. Oxford: William Andrew Publishing, 2012, pp. 87 – 125. [Online]. Available: <http://www.sciencedirect.com/science/article/pii/B9781437734553000043>

APPENDIX. CODE LISTINGS

```

Clear[s]
Clear[ic, iw, rs, rp, Zw, Zc, u, eq1, sol1]
Clear[Ac, Bc, Cc, dc, sXc, Xc, Yc]
Clear[Aw, Bw, Cw, dw, sXw, Xw, Yw]
Clear[eq2, sol2]
Clear[rels2, gb2]
eq1 = {ic*Zc[s] == iw*(rp + Zw[s]), u == rs*(ic + iw) + ic*Zc[s],
Yc == Zc[s]*ic, Yw == Zw[s]*iw};
eq1 // TableForm;
sol1 = Solve[eq1, {ic, iw, Zc[s], Zw[s]}][[1]];
sol1 // Simplify // TableForm
SetNonCommutative[Ac, Bc, Cc, Xc, sXc]
SetNonCommutative[Aw, Bw, Cw, Xw, sXw]
SetMonomialOrder[{Ac, Bc, Cc, Xc, Aw, Bw, Cw, Xw}, {sXc, sXw}];
rels2 = {-sXc + Ac ** Xc + ic*Bc, -Yc + Cc ** Xc + dc*ic, -sXw +
Aw ** Xw + iw*Bw, -Yw + Cw ** Xw + dw*iw};
rels2 = rels2 /. sol1;
rels2 // Simplify // TableForm
PrintMonomialOrder[];
gb2 = NCMakeGB[rels2, 120];
gb2 // TableForm;
eq2 = {Cc ** Xc == (Cc ** Xc /. gb2), Cw ** Xw == (Cw ** Xw /. gb2)};
eq2 // TableForm;
sol2 = Solve[eq2, {Yc, Yw}][[1]] // Simplify;
sol2 // TableForm;
SetMonomialOrder[{Ac, Bc, Cc, Xc, Aw, Bw, Cw, Xw}, {sXc, sXw}];
eqs2 = {sXc == (sXc /. gb2), sXw == (sXw /. gb2)} /. sol2;
eqs2 // TableForm;
eqs2 = Simplify[eqs2];
eqs2 // TableForm
sol2 // TableForm
((ic + iw) /. sol1) /. sol2 // Simplify

```

Listing A.1. Mathematica symbolic simplification script. Confirms non-commutative simplification of Randles cell state-space relations. Utilizes the Non-Commutative Algebra and Gröbner Basis packages.

```

function [A,B,C,D] = makeCPE(phi, sigma, omega0, omega1, delta_phi)
C1 = 1;
R1 = 1/(C1*omega0);
Dp = sigma;
ab = 0.24/(1+(delta_phi*180/pi));
m = ceil((log10(omega0)-log10(omega1))/log10(ab));
alpha = -phi*2/pi;
a = real(10^(alpha*log10(ab))); b = ab/a;
k = 1:m;
Rk = R1*a.^(k-1);
Ck = C1*b.^(k-1);
Rs = R1*a^m/(1-a); Cs = C1*(1-b)/b;
omega_av = (a/b)^(1/4)*(1/(R1*C1*ab^(ceil(m/2)-1)));
Z_av = abs(Rs + sum(Rk'./(1+1j*omega_av.*(Rk'.*Ck')))) + 1./(Cs*1j*omega_av));
Da = Z_av*(omega_av^(alpha));
DpD = Dp/Da;
Rk = DpD*Rk; Ck = Ck./DpD;
Rs = DpD*Rs; Cs = Cs./DpD;
P = [0 -1./(Rk.*Ck)]; R = [1/Cs 1./Ck];
A = diag(P); B = ones(length(P),1); C = R; D = Rs;
end

```

Listing A.2. MATLAB script for constructing a state-space approximation of a CPE using the method described by Valsa et al. [2].

```

clc; close all; clearvars;
% latex_style = {};
% latex_style(:,1) = {'interpreter', 'latex'};

%Fs = 20e3;
f=logspace(-3,3,50e3);

MRs = [20 20 10 10]; MRp = [250 250 300 1e3];
MCdl = [40*10^(-6) 40*10^(-6) 1*10^(-4) 40*10^(-6)];
Msigma = [.01 10 50 150];

% make pretty
axis_settings_nyquist = zeros(4,4);
axis_settings_nyquist(1, :) = [0 300 0 150];
axis_settings_nyquist(2, :) = [0 400 0 170];
axis_settings_nyquist(3, :) = [0 800 0 500];
axis_settings_nyquist(4, :) = [0 2500 0 1600];

yticks_settings_error = zeros(4,3);
yticks_settings_error(1, :) = [-11, -5, 3];
yticks_settings_error(2, :) = [-8, -2, 3];
yticks_settings_error(3, :) = [-7, -1, 3];
yticks_settings_error(4, :) = [-7, -1, 3];

for i=(1:4)

Rs = MRs(i); Rp = MRp(i); Cdl = MCdl(i);
sigma = Msigma(i);
Ds = sqrt(2)*sigma;

Zw = @(s) sqrt(2)*sigma*s.^(-0.5);
Zt = @(s) Rs + 1./((Cdl*s + 1./(Rp + Zw(s))));
GZdata = Zt(1j*2*pi*f);
Gdata = 1./GZdata;

[Aw,Bw,Cw,Dw] = makeCPE(-pi/4, Ds, 1e-3*2*pi, 2e3*2*pi, 8e-4);
Ac = 0; Bc = 1; Cc = 1/Cdl; Dc = 0;
k = 1/((Dw+Rp)*Rs+Dc*(Dw+Rp+Rs));
A = [
Ac - k*(Dw+Rp+Rs)*Bc*Cc,          k*Rs*Bc*Cw;
k*Rs*Bw*Cc,                      Aw - k*(Dc+Rs)*Bw*Cw
];
B = [
k*(Dw+Rp)*Bc;
k*Dc*Bw
];
C = k*[-(Dw+Rp)*Cc, -Dc*Cw];
D = k*(Dc+Dw+Rp);

```

```

G=ss(A,B,C,D);
[z,p,k] = zpndata(G);
z = cell2mat(z); p = cell2mat(p);
H = zp(z,p,k);

Hdata = squeeze(freqresp(H,1j*2*pi*f));
HZdata = 1./Hdata;

% plot the error (theoretical - model)
figure

loglog(f,abs(GZdata.' - HZdata)./abs(GZdata.'),'color','k');
axis([1e-3 1e3 ylim]); grid on;
if i==2
ybot = min(ylim);
axis([1e-3 1e3 ybot .1]); grid on;
end
title(sprintf('Case %d', i));
xlabel('$f$ Hz');
ylabel('Norm Error');
latex_fig(5.5, 4, [.12 .17 .83 .75])
xticks(logspace(-3,3,7))
yticks(logspace(...
yticks_settings_error(i, 1), ...
yticks_settings_error(i, 2), ...
yticks_settings_error(i, 3) ...
))
y_tic_exp = linspace(...
yticks_settings_error(i, 1), ...
yticks_settings_error(i, 2), ...
yticks_settings_error(i, 3) ...
);
num_y_tic_exp = length(y_tic_exp);
y_tic_labels = cell(num_y_tic_exp, 1);

% Nyquist Plot
figure
plot(real(HZdata), -imag(HZdata), 'color', 'k');
% grid on;
title(sprintf('Case %d', i));
xlabel('$\Re\{Z_m(2\pi f)\}$');
ylabel('$-\Im\{Z_m(2\pi f)\}$');
latex_fig(5.5, 4, [.12 .17 .83 .75])
axis(axis_settings_nyquist(i, :))

```

```

y_tics = yticks;
num_y_tics = length(y_tics);
y_tic_labels = cell(num_y_tics, 1);
for j=1:num_y_tics
y_tic_labels{j} = sprintf('%1$d', y_tics(j));
end
yticklabels(y_tic_labels)
save_psfraq(sprintf('nyquist%d', i))
end

```

Listing A.3. Script in MATLAB for comparing the continuous-time state-space model to the theoretical ideal.

```

function [zz, pz, kz] = MakeDiscrete(z,p,k,T)
    zz = exp(T*z); pz = exp(T*p);
    sc = 1j;
    zc = exp(T*sc);
    q = k*prod(abs(sc-z))/prod(abs(sc-p));
    r = prod(abs(zc-zz))/prod(abs(zc-pz));
    kz = q/r;
end

```

Listing A.4. Discretization MATLAB script which takes s -domain poles/zeros and overall gain and maps them to the z -domain by means of the matched z transform.


```

function [new_z, new_p, new_k] = pzPair1(z,p,k)
    m = length(z);
    n = length(p);
    remaining_z = [z];
    remaining_p = [p];

    [~, indecies] = sort(abs(remaining_p), 'descend');
    remaining_p = remaining_p(indecies);

    new_z = zeros(m,1);
    new_p = zeros(n,1);

    for i=1:n
        current_p = remaining_p(i);
        if ~isempty(remaining_z)
            closest_dist = Inf;
            closest_index = 0;
            for j=1:length(remaining_z)
                current_z = remaining_z(j);
                dist = abs(current_p - current_z);
                if dist < closest_dist
                    closest_dist = dist;
                    closest_index = j;
                end
            end
            new_z(i) = remaining_z(closest_index);
            remaining_z(closest_index) = [];
        end
        new_p(i) = current_p;
    end

    n = length(new_p);
    new_k = (k^(1/n))*ones(n,1);
end

```

Listing A.5. Script in MATLAB to pair poles/zeros and distribute gains evenly across subfilters.

```

clc; close all; clearvars;
latex_style = {};
latex_style(:,1) = {'interpreter', 'latex'};
latex_style(:,2) = {'fontsize', 14};

Fs = 20e3;
f=logspace(-3,3,50e3);
nRes = 32;

MRs = [20 20 10 10]; MRp = [250 250 300 1e3];
MCdl = [40*10^(-6) 40*10^(-6) 1*10^(-4) 40*10^(-6)];
Msigma = [.01 10 50 150];

for i=(1:4)

    Rs = MRs(i); Rp = MRp(i); Cdl = MCdl(i);
    sigma = Msigma(i);
    Ds = sqrt(2)*sigma;

    Zw = @(s) sqrt(2)*sigma*s.^(-0.5);
    Zt = @(s) Rs + 1./(Cdl*s + 1./(Rp + Zw(s)));
    GZdata = Zt(1j*2*pi*f);
    Gdata = 1./GZdata;

    [Aw,Bw,Cw,Dw] = makeCPE(-pi/4, Ds, 1e-3*2*pi, 2e3*2*pi, 8e-4);
    Ac = 0; Bc = 1; Cc = 1/Cdl; Dc = 0;
    k = 1/((Dw+Rp)*Rs+Dc*(Dw+Rp+Rs));
    A = [
    Ac - k*(Dw+Rp+Rs)*Bc*Cc,          k*Rs*Bc*Cw;
    k*Rs*Bw*Cc,                      Aw - k*(Dc+Rs)*Bw*Cw
    ];
    B = [
    k*(Dw+Rp)*Bc;
    k*Dc*Bw
    ];
    C = k*[-(Dw+Rp)*Cc, -Dc*Cw];
    D = k*(Dc+Dw+Rp);

    G=ss(A,B,C,D);

    [z,p,k] = zpkdata(G);
    z = cell2mat(z); p = cell2mat(p);
    H = zpk(z,p,k);
    Hdata = squeeze(freqresp(H,1j*2*pi*f));
    Zdata = 1./Hdata;

```

```

[zz, pz, kz] = MakeDiscrete(z,p,k,1/Fs);
HZ = zp(zz,pz,kz,1/Fs);
[nz, np, nk] = pzPair1(zz,pz,kz);
HZdata = squeeze(freqresp(HZ,exp(1j*2*pi*f/Fs)));
ZZdata = 1./HZdata;
nz=num2fixpt(nz, ufix(nRes), 2^-(nRes-1));
np=num2fixpt(np, ufix(nRes), 2^-(nRes-1));
nk=num2fixpt(nk, ufix(nRes), 2^-(nRes-1));
toRemove=(np==nz);
nz(toRemove)=[]; np(toRemove)=[]; nk(toRemove)=[];
nz(nz==0)=(2^(nRes)-1)*2^-(nRes);
np(np==0)=(2^(nRes)-1)*2^-(nRes);
nk = k^(1/length(nk))*ones(length(nk),1);
m = length(np);
HBiZdata = ones(length(f),1)';
Omega = exp(f*2*pi*1j/Fs);
for j=1:m
    HBiZdata = HBiZdata.* nk(j).*(1-nz(j)).*(1./Omega)...
        ./((1-np(j)).*(1./Omega));
end
if i==1
    figure
    latex_fig(3.2, 3, [.12 .17 .83 .75])
    theta = 0:pi/500:2*pi;
    xunit = cos(theta);
    yunit = sin(theta);
    plot(xunit, yunit,'color','k','LineWidth', 1);
    line(xlim, [0 0], 'color','k','linestyle',':');
    line([0 0], ylim, 'color','k','linestyle',':');
    axis(1.05*[-1 1 -1 1])
    title(sprintf('Case %d', i));
    xlabel('$\text{Real}\{z\}$');
    ylabel('$-\text{Imag}\{z\}$');
    pbaspect([1 1 1])
    colormap(jet)
    hold on;
    for j=1:m
        cur_z = nz(j);
        cur_p = np(j);
        %color = colors(j,:);
        color = (0.15+0.3-0.3*(j/m))*[1 1 1];
        scatter(real(cur_z),imag(cur_z),75,color,'o','LineWidth', 1);
        scatter(real(cur_p),imag(cur_p),75,color,'x','LineWidth', 1);
    end
    hold off;
    save_psfrag(sprintf('fppzinit'))
end
end

```

```

figure
latex_fig(3.2, 3, [.12 .17 .83 .75])
theta = 0:pi/500:2*pi;
xunit = cos(theta);
yunit = sin(theta);
plot(xunit, yunit, 'color', 'k', 'LineWidth', 1);
line(xlim, [0 0], 'color', 'k', 'linestyle', ':');
line([0 0], ylim, 'color', 'k', 'linestyle', ':');
axis([0.8305 1.0051 -0.0873 0.0873])
title(sprintf('Case %d', i));
xlabel('$\text{Real}\{z\}$');
ylabel('$-\text{Imag}\{z\}$');
pbaspect([1 1 1])
hold on;
for j=1:m
    cur_z = nz(j);
    cur_p = np(j);
    color = (0.15+0.3-0.3*(j/m))*[1 1 1];
    scatter(real(cur_z), imag(cur_z), 75, color, 'o', 'LineWidth', .5);
    scatter(real(cur_p), imag(cur_p), 75, color, 'x', 'LineWidth', .5);
end
hold off;
save_psfrag(sprintf('fppz%d', i))

figure
op1=[-0.080510752688172, 0.46797014826023,
    1.158357771260996, 0.444269433753729];
op2=[-0.080510752688172, 0.003464040717085,
    1.158357771261, 0.443618090927728];
pp1=[0.0701, 0.5738, 0.8977, 0.2843];
pp2=[0.070075757575758, 0.108851068642252, 0.897727272727275, 0.284345003479959];
latex_fig(6.3, 4, [.8 .12 .90 .75])
sgtitle(sprintf('Case %d', i));
subplot(211)
ax=gca;
ax.OuterPosition = op1;
ax.Position = pp1;

semilogx(f, abs(HBiZdata), 'color', 'k'); hold on;
semilogx(f, abs(Gdata), 'color', 'k', 'linestyle', ':');
legend({'Digital Model', 'Theoretical Model'}, 'Location', 'northwest');
title('$\text{ITAbs}$')
xlabel('Hz');
subplot(212);
semilogx(f, 180/pi*angle(HBiZdata), 'color', 'k'); hold on;
semilogx(f, 180/pi*angle(Gdata), 'color', 'k', 'linestyle', ':');
legend({'Digital Model', 'Theoretical Model'}, 'Location', 'northwest');
title('$\text{ITPhs}$');

```

```
xlabel('Hz');  
ax=gca;  
ax.OuterPosition = op2;  
ax.Position = pp2;  
  
save_psfraq(sprintf('fpresp%d', i))  
  
end
```

Listing A.6. Script in MATLAB for analyze the effects of fixed-point approximations to the discretized model.